Characterization of bituminite in Kimmeridge Clay by confocal laser scanning and atomic force microscopy

Paul C. Hackley [a,*], Jolanta Kus [b], João Graciano Mendonça Filho [c], Andrew D. Czaja [d], Angeles G. Borrego [e], Dragana Životić [f], Brett J. Valentine [a], Javin J. Hatcherian [a]

[a] *U.S. Geological Survey (USGS), United States of America*
[b] *BGR, Germany*
[c] *UFRJ, Brazil*
[d] *Univ. Cincinnati, United States of America*
[e] *INCAR-CSIC, Spain*
[f] *Univ. Belgrade, Serbia*

ARTICLE INFO

ABSTRACT

This work investigates bituminite (amorphous sedimentary organic matter) in Upper Jurassic Kimmeridge Clay source rock via confocal laser scanning microscopy (CLSM) and atomic force microscopy (AFM). These petrographic tools were used to provide better understanding of the nature of bituminite, which has been historically difficult to identify and differentiate from similar organic matter types in source rocks. As part of an International Committee for Coal and Organic Petrology (ICCP) working group, an immature (0.42% vitrinite reflectance), organic-rich (44.1 wt% total organic carbon content) sample of Kimmeridge Clay was distributed to multiple laboratories for CLSM characterization. The primary observations from CLSM imaging and spectroscopy include: 1) the interpreted presence of *Botryococcus* algae as a contributor to bituminite precursors; 2) color red-shift of sulfide reflectance and bituminite auto-fluorescence from below the sample surface; 3) positive alteration of bituminite from laser-induced photo-oxidation of the sample surface, including fluorescence blue-shift; 4) fluorescence blue-shift associated to higher fluorescence intensity regions in bituminite indicative of compositional (fluorophore) differences; 5) the need for fluorescence spectroscopy standardization as applied via CLSM; and 6) the suitability of CLSM fluorescence spectroscopy to predict solid bitumen reflectance from bituminite spectral emission via calibration to an extant dataset. Secondary CLSM observations include detection of reflected laser light from highly reflective inclusions in bituminite, including sulfides and fusinite, and radiolytic alteration of bituminite caused by substitution of U for Fe in sulfides. Findings from AFM include the observation that surface roughening or surface flattening of bituminite are induced by differential broad ion beam (BIB) milling and are dependent on the location and scale of AFM topology measurement. This result highlights our still limited understanding of the effects of BIB milling on sedimentary organic matter and indicates the need for further research before this technique can be advanced as a standard practice in petrographic sample preparation. Collectively, the results of this study illustrate the general applicability and versatility of AFM and CLSM as tools for organic petrology research, specifically for better understanding of the nature and properties of the bituminite maceral.

1. Introduction

Bituminite is unstructured (amorphous) sedimentary organic matter with no specific or distinct form (Pickel et al., 2017; Taylor et al., 1998). Because of the absence of form, and the general infidelity of organic petrographers to its accepted description, bituminite has been historically difficult to identify reproducibly in interlaboratory studies (Kus et al., 2017). Nevertheless, its characterization is important in a petroleum systems context, as its hydrogen-rich nature means that it typically constitutes the primary contribution to hydrocarbon generation from

oil-prone source rocks during thermal advance (Hutton et al., 1980; Teichmüller, 1974a). This oil-prone character is suggested by its name (Teichmüller, 1971) and its primary source as preserved lipids from algal and bacterial organic matter (Boussafir et al., 1995; Hutton et al., 1994), although a range of other precursor organisms have been suggested including humic plant derivatives, fungi and higher animals [summarized in Pickel et al., 2017].

Bituminite is a maceral in the liptinite group, and a common component of the organic matter fraction in unconsolidated sediments or in immature to marginally mature petroleum source rocks. In white light under oil immersion, bituminite occurs typically as black, dark brown, or reddish tinted, poorly-reflecting organic matter with red internal reflections and common mineral inclusions, and texturally as wispy or ropy laminae, irregular streaks and threads (Botz et al., 2007; Boucsein and Stein, 2009; Eble, 2012; Fishman et al., 2012; Geršlová et al., 2015; Hackley et al., 2016; Hackley and SanFilipo, 2016; Kolonic et al., 2002; Kus et al., 2017; Nowak, 2007; Pickel et al., 2017; Rimmer et al., 2004; Ross and Bustin, 2006; Stasiuk, 1993; Stasiuk and Goodarzi, 1988; Synnott et al., 2017; Tao et al., 2012; Taylor et al., 1991; Teng et al., 2021). Its fluorescence character is variable, ranging from brightly fluorescent to non-fluorescent (Pickel et al., 2017; Powell et al., 1982; Teichmüller and Ottenjann, 1977). Several workers have attempted to subdivide bituminite types into a classification scheme based on its optical properties, e.g., reflectance, color, and fluorescence character (Creaney, 1980; Mukhopadhyay et al., 1985; Teichmüller and Ottenjann, 1977; van Gijzel, 1981). However, the wide variation in presentation of the optical properties of bituminite is responsible for difficulties in its reproducible identification. Using the results of three interlaboratory studies, Kus et al. (2017) found that identification of bituminite was inhibited for three primary reasons: (1) similarity and association to liptinite maceral lamalginite; (2) similarity and association with fluorescent mineral bituminous groundmass (a variable mixture of fine-grained organic and inorganic material); and (3) lack of a 'fine granular texture,' which has been cited as a typical identifying feature of bituminite (Taylor et al., 1998). The association of bituminite with lamalginite and mineral bituminous groundmass was further examined by Hackley et al. (2018), who suggested that bituminite occurs in a continuum with mineral bituminous groundmass subject to the relative degree of mineral dilution, and in a continuum with lamalginite subject to the relative degree of bacterial or oxidative degradation. Furthermore, Hackley et al. (2018) suggested bituminite occurs in continuum with petrographic solid bitumen (a solid petroleum) subject to the relative degree of thermal advance. This continuum (between the organic components bituminite, lamalginite, mineral bituminous groundmass, and solid bitumen) may manifest within a single microscope field, illustrating the relative complexity of source rock organic petrology and suggesting that state-of-the-art microscopy tools are necessary to increase the pace of innovation in this field.

Confocal laser scanning microscopy (CLSM) and atomic force microscopy (AFM) are advanced microscopy techniques with increasing applications for organic petrology investigations over the last decade (Hackley et al., 2021; Kus, 2015; Wang et al., 2021). CLSM detects fluorescence response from a sample by rastering a laser over the scan area and using a spatial pinhole to discard out of focus light (Webb, 1996). This technique has multiple applications in organic petrology and geobiology, including two-dimensional imaging (Kus, 2015; Nix and Feist-Burkhardt, 2003; Stasiuk, 1999; Stasiuk and Sanei, 2001), three-dimensional imaging (Czaja et al., 2016; Schopf and Kudryavtsev, 2009; Schopf et al., 2010; Schopf et al., 2011; Schopf et al., 2016), and fluorescence spectroscopy (Hackley et al., 2020a; Hackley and Kus, 2015; Kus et al., 2016). AFM utilizes a fine-tipped cantilever, the movement of which is monitored by a laser as it experiences surface force interactions with the sample (Binnig et al., 1986). The AFM is operated in several modes (contact, tapping, non-contact), which generate multiple data output formats (e.g., topology, elasticity, hardness, adhesion, surface charge density) that are useful for organic

petrology and geobiology investigations (Eliyahu et al., 2015; Emmanuel et al., 2016; Hackley et al., 2020b; Kempe et al., 2002; Pacton et al., 2007).

Herein, we present information from AFM and CLSM analyses of bituminite in a sample of the Upper Jurassic Kimmeridge Clay Formation. The work was conducted under the auspices of the International Committee for Coal and Organic Petrology (ICCP) within a working group tasked with the general objective to investigate current applications of CLSM to organic petrology investigations. Bituminite was selected as the object of study due to the known historical issues with its identification and characterization (Kus et al., 2017), and because of complementary ongoing work in other ICCP working groups. A bituminite-rich sample from the Blackstone layer of the Kimmeridge Clay Formation (Boussafir et al., 1995; Williams and Douglas, 1980), which had been previously characterized for other works (Birdwell and Washburn, 2015; Bolin et al., 2016; Hackley et al., 2018; Valentine et al., 2019), was selected as the object of study. The motivation for this work was to highlight the types of information that advanced microscopy tools such as CLSM and AFM can generate and apply to understanding the nature of bituminite; for example, the determination of approximate thermal maturity via fluorescence spectroscopy.

2. Materials and methods

2.1. Sample

The Upper Jurassic Kimmeridge Clay Formation sample (sample ID KC-1) studied herein was collected from the Blackstone oil shale layer on the Dorset coast of southern England in the Wessex Basin (coordinates 50.5975, −2.0930), near the town of Kimmeridge, between Kimmeridge Bay and Chapmans Pool. The sample contains approximately 44 wt% total organic carbon content (Hackley et al., 2018), mostly comprised of fluorescent bituminite.

2.2. Sample preparation

The KC-1 sample was prepared via typical procedures (ASTM, 2015a) in a thermoplastic whole-rock mount and mechanically polished to a finish of 0.05 μm, prior to distribution. Kerogen isolation to separate bituminite from mineral matrix was performed using standard non-oxidative procedures according to Mendonça Filho et al. (2017). Briefly, each sample was crushed to approximately 2 mm size and subjected to an acid treatment to remove carbonates (HCl 37% for 18 h), silicates (HF 40% for 24 h), and neoformed fluorides (HCl 37% for 3 h). Between each acid treatment, the pH of the residue was neutralized with filtered water. Organic and non-organic fractions were separated by flotation using $ZnCl_2$ (density = 1.9 to 2 g/cm^3). The organic fraction was recovered, and the heavy liquid was eliminated using drops of HCl (10%) followed by a wash with filtered water. The isolated kerogen was sieved at 10 μm. Strew slides and kerogen concentrate mounts were prepared via typical procedures (e.g., Tyson, 1995). Broad ion beam milling of the mechanically polished sample used two approaches: 1) a Hitachi IM 4000 Plus ion mill operated for 5 min, using 4 keV; 15°incline; 360° rotation at 25 rpm; 100% focus (1.5 kV discharge; ~100 μA), and 2) an E.A. Fischione 1060 ion mill operated with beam conditions of 6 keV, 2° gun angle, 175° rotation at 3 rpm, 50% focus, for 30 min.

2.3. Organic petrography

The organic petrography of the KC-1 sample has been summarized in previous work (Hackley et al., 2018; Valentine et al., 2019) but is briefly revisited here for context. Qualitative organic petrography analysis (at U.S. Geological Survey, USGS) was conducted on Zeiss AxioImager or Leica DM 4000 microscopes using 50× oil immersion objectives under incident white light or epi-fluorescence. Bituminite has a reddish tint (in

incident white light; Fig. 1A) and lacks a gray reflecting surface after typical mechanical polish (to a finish of 0.05 μm). Dispersed terrigenous inertinite is common and vitrinite is present in trace amounts. Scattered sporinite and discrete telalginite bodies are sparse. Some micrinite is present from early conversion of the bituminite (Teichmüller, 1974b), or due to diffuse light scattering from dispersed clay minerals (Faraj and Mackinnon, 1993). Radiation alteration halos are present as zones of red-shifted and diminished fluorescence intensity (Zheng et al., 2021) surrounding heavy minerals (?) and sulfides embedded in the bituminite (Fig. 1B). Although radiolytic damage to sedimentary organic matter usually causes an increase of organic reflectance (e.g., Luo et al., 2014; Machovic et al., 2021), this effect was not observed in bituminite. Reflectance measurements (at USGS) were completed on a Leica DM 4000 microscope with LED illumination and a monochrome camera for light detection operated by the computer program DISKUS-FOSSIL from Hilgers Technisches Buero. Calibration of the microscope used a yttrium-aluminum-garnet (YAG) reflectance standard (0.908% R_o) from Klein & Becker. Mean reflectance determined via ASTM 7708 (ASTM, 2015b) of scarce solid bitumen (BR_o) is 0.29% (s.d. 0.03, n = 13, Hackley et al., 2018), whereas mean vitrinite reflectance (VR_o) is 0.42% (s.d. 0.03, n = 13). Mean reflectance of the bituminite is 0.16% (s.d. 0.02, n = 55, Valentine et al., 2019). The relative reflectance values of vitrinite (0.42%), solid bitumen (0.29%), and bituminite (0.16%) are consistent with an intuitive correlation to their expected H/C ratios (Burnham, 2019), although in situ H/C measurements are not available for the individual macerals. A white to red (in incident white light;

Fig. 1C) sulfide and its weathering products occur as framboids, replacing shell (fossilized bone?), and the weathering products (goethite plus carbonate?) show long wavelength fluorescence (Fig. 1D). Unaltered pyrite framboids are common.

2.4. Confocal laser scanning microscopy

Confocal laser scanning microscopy was performed in multiple laboratories using different instrument systems and data collection parameters. This information is compiled in Table 1 and reiterated in the results section where appropriate.

2.5. Atomic force microscopy

Atomic force microscopy (AFM) at Hitachi used a Hitachi AFM5500M system with commercial silicon cantilevers having manufacturer nominal values of 10 nm for tip radius, 125 μm length, and 4 N/m spring constant operated in contact mode. AFM at Keysight used a Keysight Technologies 9500 AFM operated in AC mode using Nanosensors PPP-NCH cantilevers (nominal k = 40 N/m, resonance frequency = 300 kHz). Images were acquired using line scan speeds around 1 Hz at 600 × 600 pixel density. AFM topology data sets were evaluated for areal root-mean-square surface roughness (S_q), the root mean square value of the ordinate values of surface height distribution (Gadelmawla et al., 2002; ISO, 2012), calculated by Formula I.
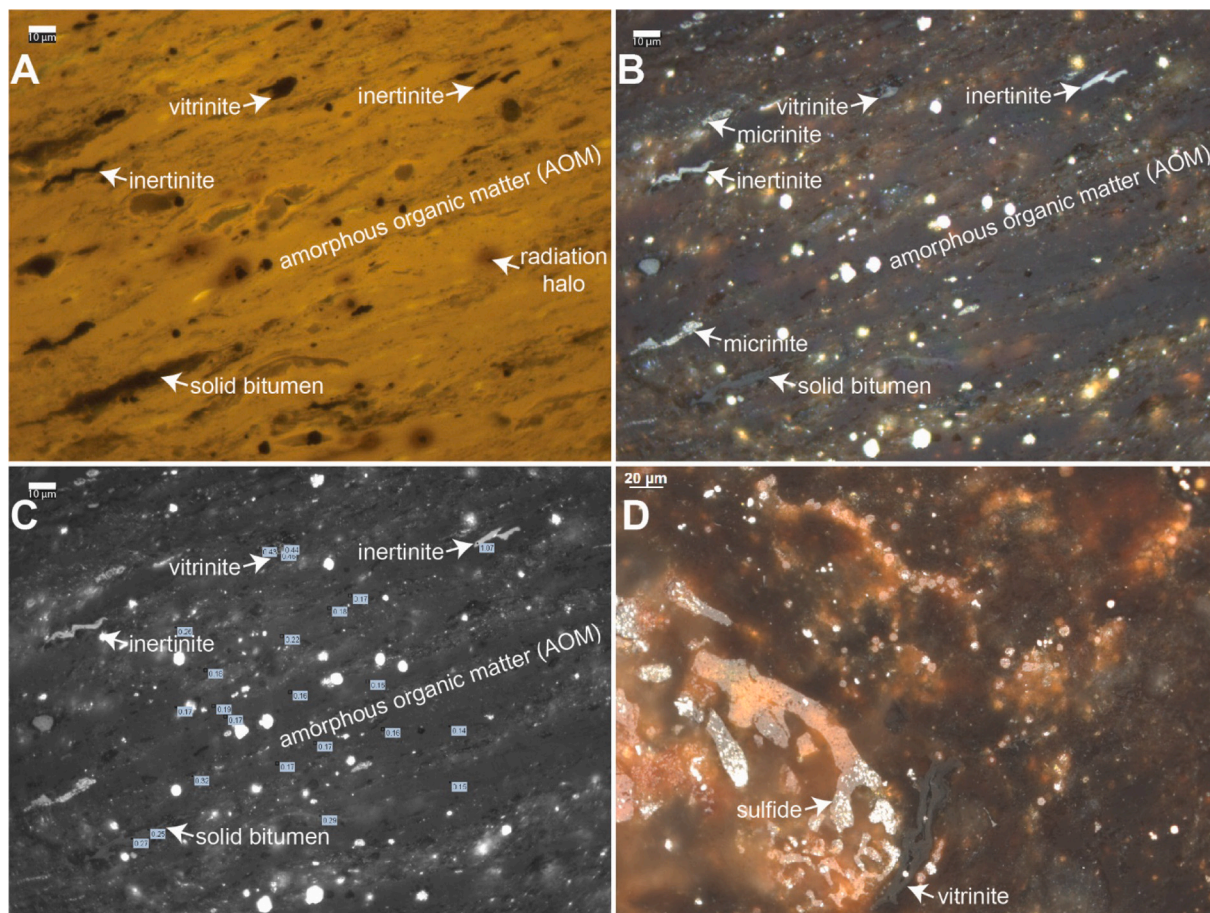

Fig. 1. Optical photomicrographs of bituminite in the KC-1 sample. A. Bituminite under epi-fluorescence showing radiation halos (decreased fluorescence intensity emission areas with color red-shift) around heavy minerals (?) and sulfides. B. Same field as A in white light (under oil immersion) showing scattered terrigenous macerals (vitrinite and inertinite). C. Same field as A-B taken with a monochrome camera showing reflectance values of selected measurement areas. D. Sulfide altering to oxidation products and replacing bone (?) under incident white light and oil immersion. (For interpretation of the references to color in this figure legend, the reader is referred to the web version of this article.)

Table 1

Confocal laser scanning microscopy locations and parameters. NA, numerical aperture.

Worker, laboratory	Instrument	Specifications
Andrew Czaja, Univ. Cincinnati	Olympus FluoView 1000	458 Ar laser; 1024 × 1024 pixel resolution; 40 μs/pixel; 4× digital zoom, 60× 1.42 NA oil obj.
Jolanta Kus, BGR	Leica TCS SP5 AOBS	458, 496, 633 nm lasers; 455–492 nm, 499–629 nm, 636–800 nm detection; 1024 × 1024 pixel resolution; 10 Hz; variable digital zoom; 63× 1.4 NA oil obj.
Paul Hackley, Univ. Maryland	Leica DMi8 SP8 AOTF	405 diode laser; xyλ scan; 415–725 nm detection; 1024 × 1024 pixel resolution; 8-bit color; 10 nm unidirectional scan steps; 400 Hz; 1 accumulation; 1 Airy unit; 63.0× 1.40 NA oil obj.
Angeles Borrego, INCAR	Leica SP5X	405 diode laser; xyλ scan.

$$S_q = \sqrt{\frac{1}{N_x N_y} \sum_{i=1}^{N_x} \sum_{j=1}^{N_y} z^2\left(x_i, y_j\right)} \qquad (I)$$

where N_x and N_y are numbers of points on the X and Y axes of each topology data set and z is height (ISO, 2012). Lower values of S_q indicate flatter surfaces.

3. Results and discussion

3.1. CLSM imaging

CLSM imaging at University of Cincinnati reveals that bituminite groundmass hosts multiple other macerals and minerals (Fig. 2).

An important observation is the distinction in fluorescence color and emission intensity between terrigenous sporinite (?) (green, high intensity) and adjacent marine bituminite (yellow, lower intensity).
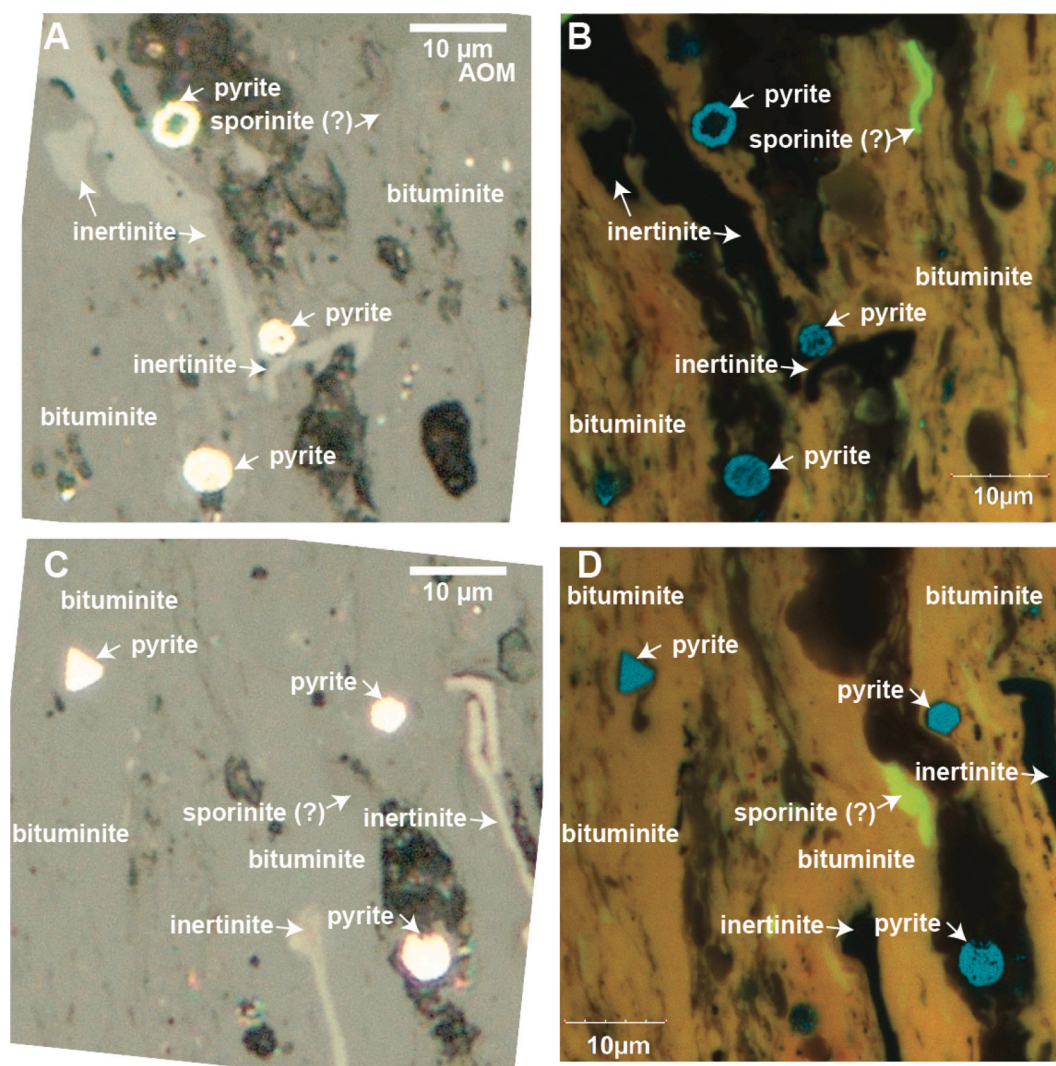

Fig. 2. Optical and 3-channel false color confocal laser scanning microscopy (CLSM) photomicrographs of bituminite in KC-1 sample from Univ. Cincinnati imaging. A. Optical image (dry 50× LWD objective) showing bituminite, pyrite, inertinite, and sporinite (?). B. Same field as A imaged via CLSM showing yellow fluorescence of bituminite, green fluorescence of sporinite (?) and blue laser (458 nm) reflection from pyrite. C. Optical image (dry objective) showing bituminite, pyrite, inertinite, and sporinite (?). D. Same field as C imaged via CLSM showing yellow fluorescence of bituminite, green fluorescence of sporinite (?) and blue laser reflection from pyrite. Note inability to differentiate sporinite (?) from bituminite in optical images A and C and the fluorescence color contrast of sporinite and bituminite in CLSM images B and D. (For interpretation of the references to color in this figure legend, the reader is referred to the web version of this article.)

Radiation damage halos are present in both CLSM images (Fig. 2B, D), as indicated by a decrease in bituminite fluorescence intensity and redshift, the same as noted in conventional fluorescence imaging (Fig. 1B). Also of note is the Ar laser (458 nm) reflection from pyrite using a 480–495 bandpass filter (Fig. 2B, D). Each CLSM image is a 3-channel composite as shown in Fig. 3; the blue color of pyrite appears to be due to incomplete blocking of 458 nm reflected laser light by the 480–495 nm bandpass filter in the cyan color channel.

CLSM imaging at BGR revealed a similar maceral assemblage as discussed above: bituminite (Fig. 4A-D), telalginite (Fig. 4A, C), inertinite (fusinite, Fig. 4B), and sporinite (Fig. 4A, C). As noted from conventional fluorescence microscopy, radiation halos occurring around blue-reflecting sulfide, or its oxidized replacement (noted by a decrease in fluorescence emission intensity and red-shift, Fig. 4B, D), may suggest some U substitution for Fe. Reflection of the blue laser line from highly reflective sulfides, as interpreted from the University of Cincinnati imaging (Fig. 2B, D; Fig. 3), is confirmed in the BGR imaging, which also shows blue laser reflection from highly reflective fusinite with distinct 'bogen' (ICCP, 2001) structure (Fig. 4B). The capture of reflected laser light at the detector in two different CLSM systems in this study suggests careful attention is necessary in the selection of filter combinations to avoid artifacts, particularly if the field of interest contains highly reflective subjects.

In contrast to the sporinite (?) identified in the University of Cincinnati images, sporinite in BGR images is interpreted to have red-shifted and lower fluorescence intensity emission compared to telalginite (Fig. 4A, C). We note that identification of structured sporinite as an included organic component or organic inclusion in bituminite highlights the improved imaging resolution offered by CLSM over conventional epi-fluorescence. Also identified in the BGR images is the presence of non-fluorescent coccospheres (Fig. 4D), as documented by previous workers (Lees et al., 2006; Lees et al., 2004). Some diagenetic
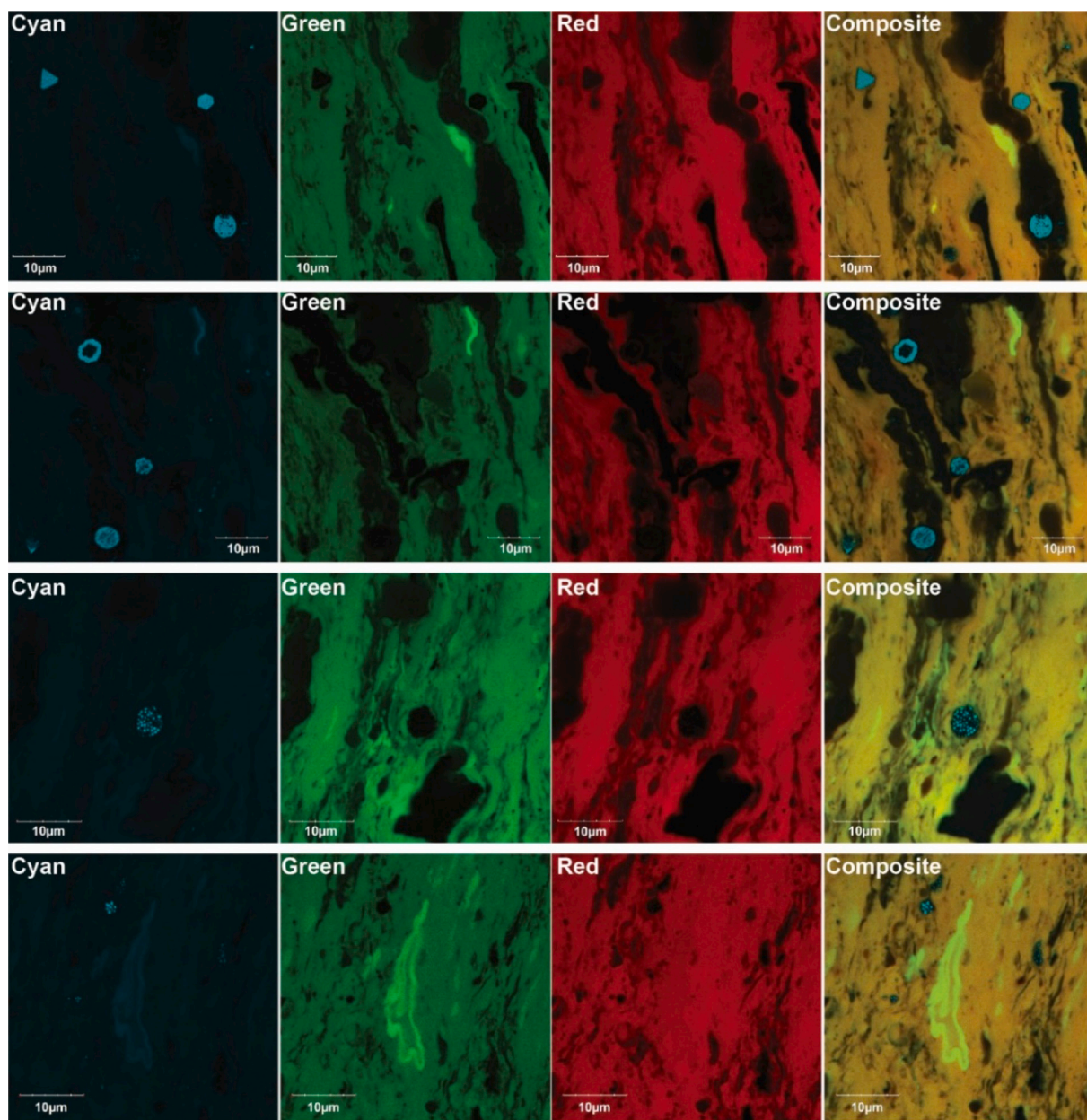

Fig. 3. Three-channel construction of confocal laser scanning false color fluorescence composite images of bituminite in the KC-1 sample from University of Cincinnati imaging. Cyan: 458 nm Ar laser, 480–495 bandpass filter. Green: 458 nm Ar laser, 535–565 bandpass filter. Red: 635 nm diode laser, 655–755 bandpass filter. (For interpretation of the references to color in this figure legend, the reader is referred to the web version of this article.)
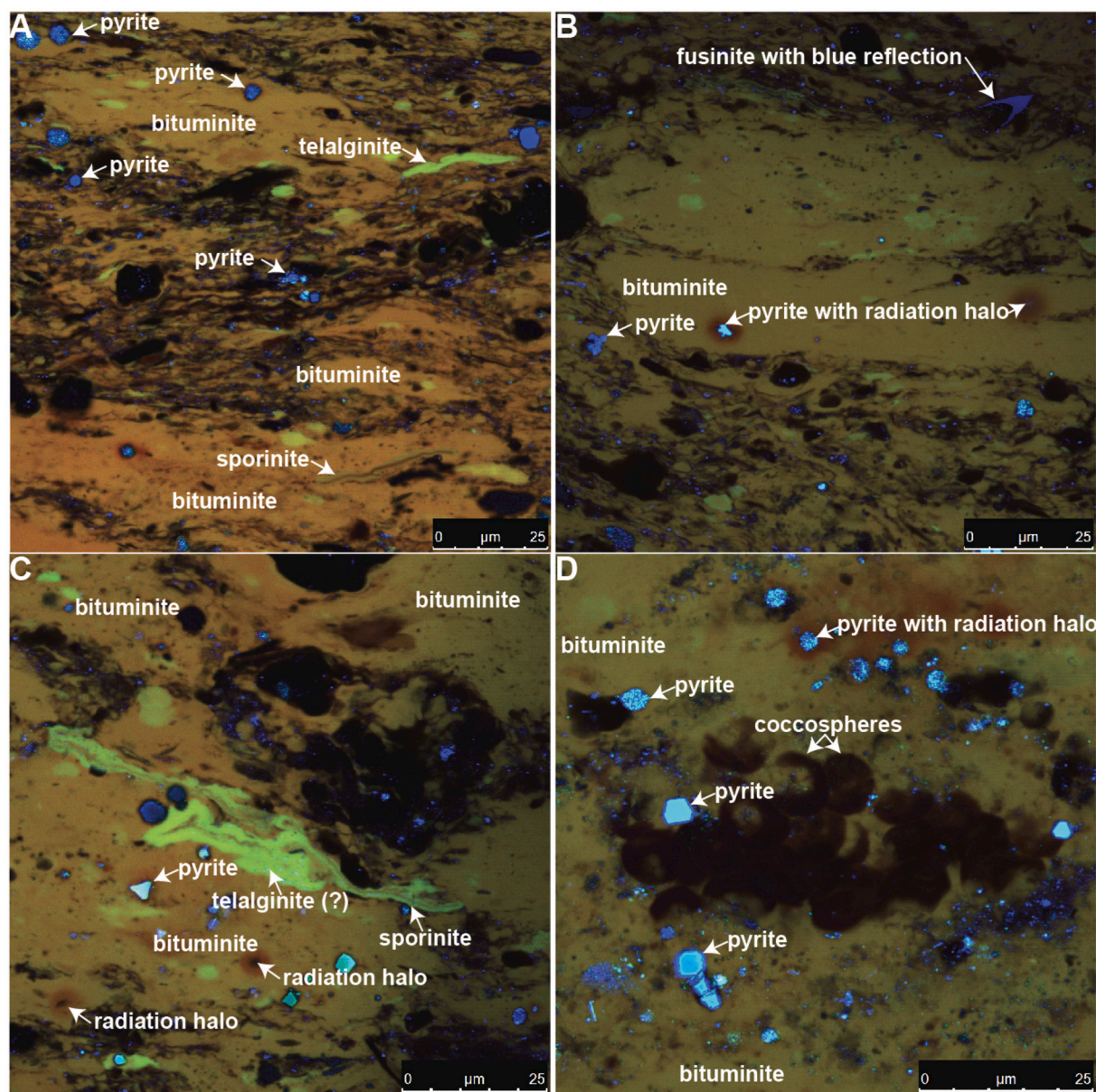
Fig. 4. Three-channel construction of confocal laser scanning microscopy (CLSM) false color fluorescence composite photomicrographs of bituminite in KC-1 sample from BGR imaging. A. Bituminite with inclusions of pyrite, telalginite, and sporinite. B. Bituminite with 'bogen' structure fusinite inclusion. C. Bituminite with inclusions of pyrite, telalginite, and sporinite. D. Bituminite with coccosphere and pyrite inclusions. CLSM images captured with oil objective 63× and 1.40 NA by application of Ar and HeNe-lasers (excitation with 458 nm, 496 nm, and 633 nm laser lines; voxel-width: A: 114.1 nm; B: 101.7 nm; C: 90.6 nm; D: 75.4 nm; scan format 1024 × 1024 pixels; digital zoom at 2.4, bidirectional scanning).

pyritization of individual coccospheres is evident as blue reflections from sulfide (Fig. 5A, B). Fluorescence imaging of bituminite from approximately 1.5 μm below the sample surface (Fig. 5C) shows a discrete red-shift in emission compared to the sample surface. Reflection (not autofluorescence) from subsurface sulfide framboids also shows red-shift with greater frequency of green (as opposed to blue) light imaged (Fig. 5C), possibly because more of the emitted photon energy is lost to frictional interaction as it passes through the sample. The fluorescence red-shift of bituminite and reflectance red-shift of pyrite can be visually compared between Fig. 5C, where bituminite and pyrite below the sample surface are red-shifted, and Fig. 5D, where bituminite in the sample surface is relatively blue-shifted, and some pyrite just below the sample surface reflects in green wavelengths compared to blue reflections at the sample surface.

An important observation in the BGR imaging is the presence of organic matter with morphology suggestive of remnants of *Botryococcus*

(Fig. 6A), a freshwater (Metzger and Largeau, 2005; Rao et al., 2007; Vandenbroucke and Largeau, 2007) to brackish, moderate-salinity green alga. The living form of *Botryococcus braunii* has been reported to occur in freshwater as well as in saltwater conditions (Masters, 1971). The interpreted presence of a moderate-salinity alga in the marine (Boussafir et al., 1995; Fishman et al., 2012; Tribovillard et al., 1994) Kimmeridge Clay Formation is contradictory, and, if correct, implies proximal deposition, such as an estuarine setting, where transported moderate-salinity algae may have accumulated. Nevertheless, the morphological preservation of *Botryococcus*-like organic matter is well-documented in Fig. 6A-B, including an example of unambiguous *Botryococcus* (from (Kus, 2015), from Visean lignite, Russia) for comparison in the inset of Fig. 6B. The visual similarity of branches and top and side openings is striking. Fig. 6A-B also provide comparison of the sample surface (Fig. 6A) and a focal plane from 2 to 3 μm below the surface (Fig. 6B), allowing further visual confirmation of fluorescence red-shift from
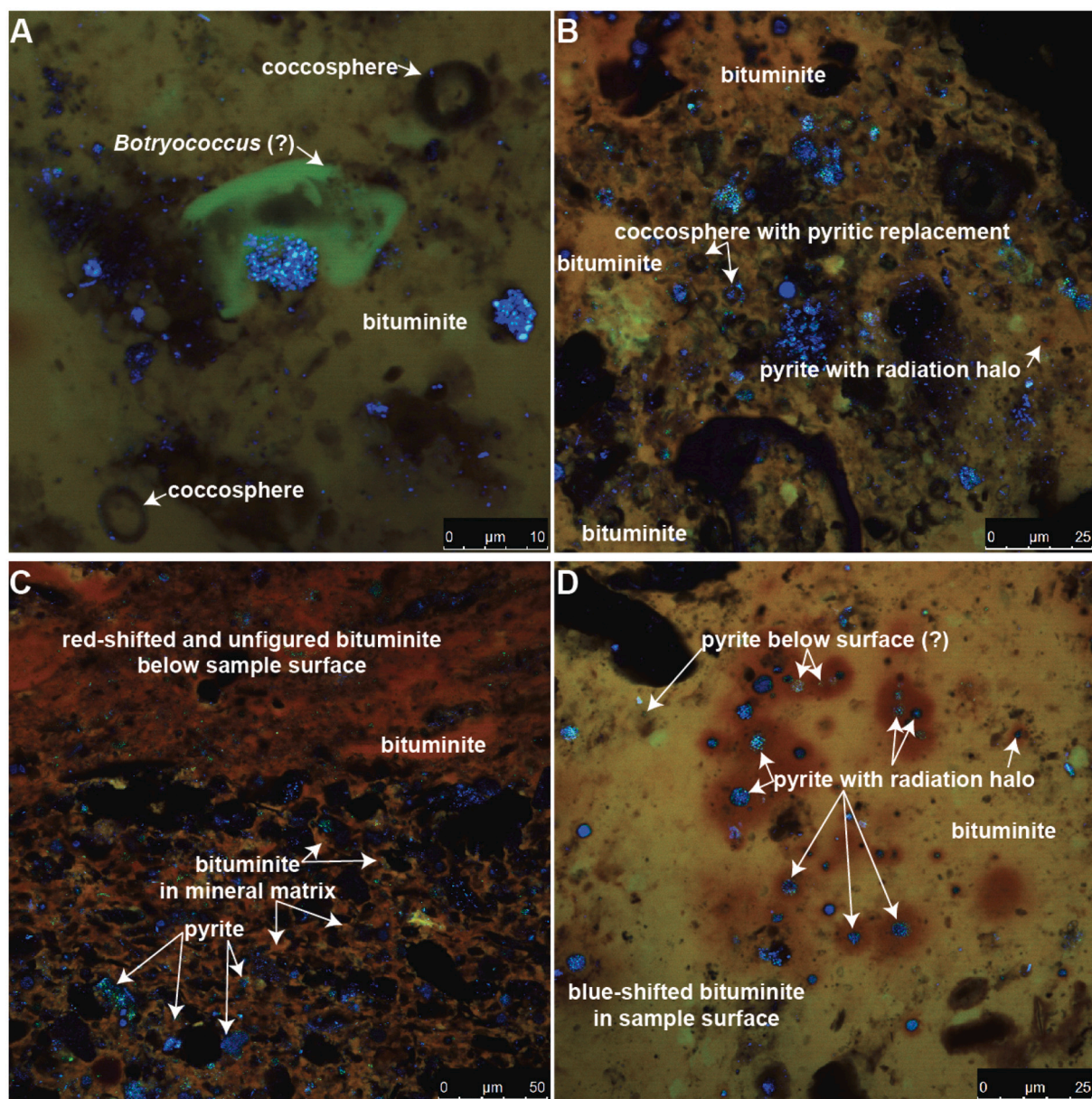
Fig. 5. Confocal laser scanning microscopy (CLSM) photomicrographs of KC-1 sample from BGR imaging. A. *Botryococcus* (?) freshwater alga and coccospheres in bituminite. B. Coccospheres (some with pyritic replacement) in bituminite. C. Red-shifted fluorescence of bituminite and reflection from pyrite approximately 1.5 μm below the sample surface. D. Radiation halos surrounding blue-laser reflecting pyrite framboids, with some red-shifted reflection from pyrite slightly below surface. CLSM photomicrographs captured with oil objective 63× and 1.40 NA by application of Ar and HeNe-lasers (excitation with 458 nm, 496 nm, and 633 nm laser lines; voxel-width: A: 50.4 nm; B: 121.8 nm; C: 240.5 nm; D: 113.7 nm; scan format 1024 × 1024 pixels; digital zoom at 2.4, bidirectional scanning). (For interpretation of the references to color in this figure legend, the reader is referred to the web version of this article.)

bituminite below the surface, and reflectance red-shift from pyrite below the surface. If the interpretation of preserved *Botryococcus* morphology is correct, it may suggest that transitional states between remnant *Botryococcus* and unfigured bituminite also may be present. Possible transitional states are indicated in the images of Fig. 6C-D, which include suggestions of preserved mottled structures, and blue-shifted areas which may be poorly preserved remnants of individual *Botryococcus* branches. The potential identification of structured *Botryococcus* remnants as a constituent of overall unstructured bituminite via CLSM again points to an improved visualization over conventional epi-fluorescence, and further highlights the importance of this high resolution and three-dimensional (3-D) imaging approach for organic petrology investigation and paleoenvironmental reconstruction.

3.2. CLSM spectroscopy

CLSM imaging and spectroscopy of the bituminite in the kerogen concentrate sample of KC-1 (Fig. 7A) at INCAR indicated the wavelength of maximum emission (λ_{max}) was approximately 562 nm (Fig. 7B). The kerogen concentrate contains other organic matter types, e.g., terrigenous macerals; however, the CLSM spectroscopy investigation specifically probed bituminite as documented in Fig. 7A and C. Using the empirical calibration of Hackley and Kus (2015), 562 nm converts to an equivalent BR_o value of 0.52%, significantly higher than either of the measured BR_o or VR_o values reported herein (0.29% and 0.42%, respectively). However, the calibration of Hackley and Kus (2015) was determined for *Tasmanites* telalginite and solid bitumen in Upper Devonian shale of the foreland Appalachian Basin e.g. (Ettensohn,
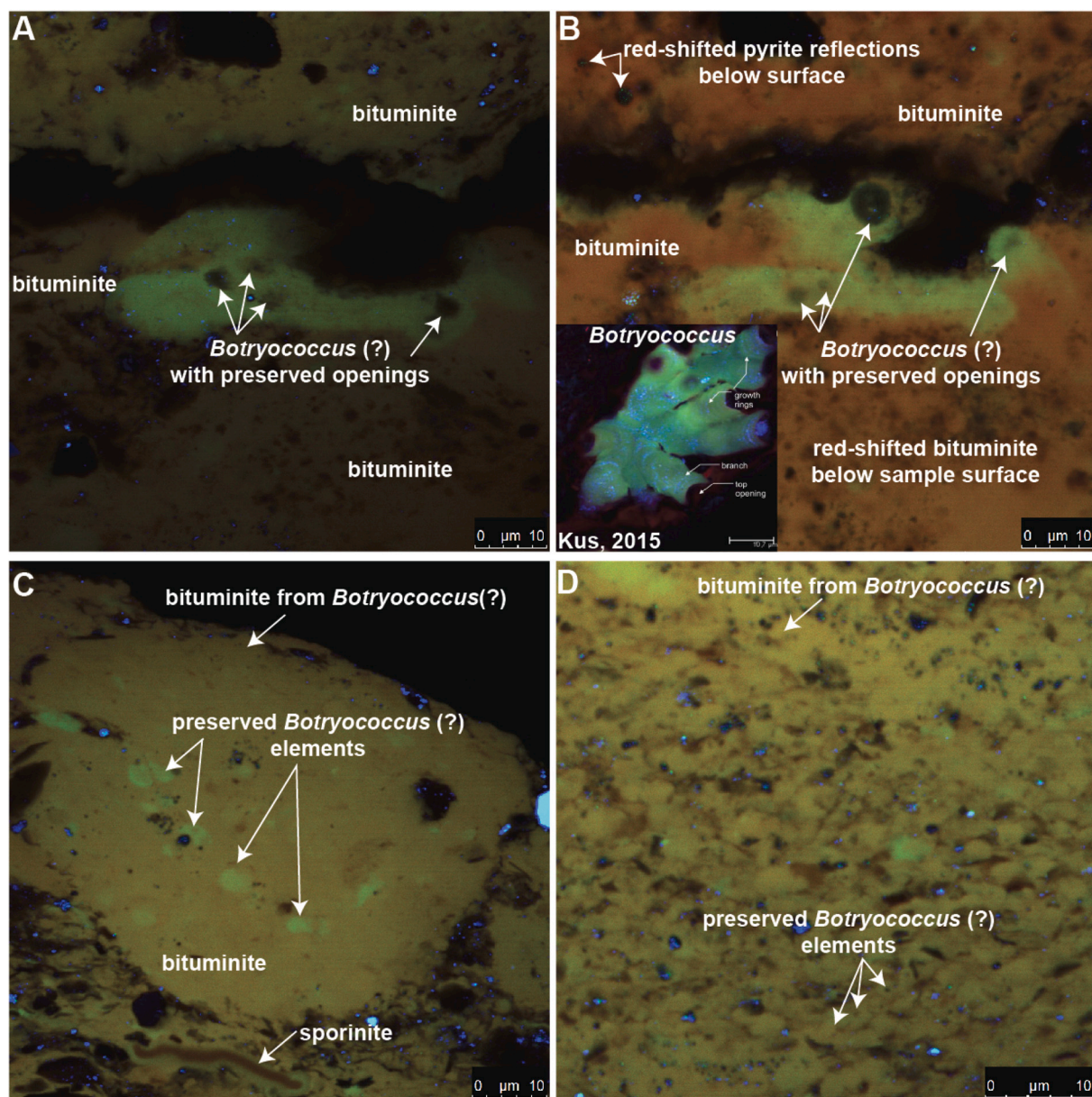
Fig. 6. Confocal laser scanning microscopy (CLSM) photomicrographs of KC-1 sample from BGR imaging. A. *Botryococcus* (?) with preserved openings. B. Same field as A but from 2 to 3 μm below the sample surface showing red-shifted bituminite fluorescence and pyrite reflection. C–D. Bituminite with some preserved *Botryococcus* (?) elements. CLSM photomicrographs captured with 63× oil objective (1.40 NA) by application of Ar and HeNe-lasers (excitation with 458 nm, 496 nm, and 633 nm laser lines; voxel-width: A: 73.0 nm; B: 73.0 nm; C: 70.3 nm; D: 48.2 nm; scan format 1024 × 1024 pixels; digital zoom at 2.4, bidirectional scanning). (For interpretation of the references to color in this figure legend, the reader is referred to the web version of this article.)

1998), a significantly different maceral type and geologic age than the Upper Jurassic sample from the rifted Wessex Basin (Chadwick, 1986) considered herein. Using an empirical calibration ($BR_o = 0.0025*\lambda_{max}$-1.1168), derived from data in (Stasiuk, 1994) for stromatolitic *Gloeocapsomorpha prisca* (*G. prisca*) alginite and co-occurring solid bitumen, results in a calculated BR_o value of 0.29%, matching the measured value for solid bitumen in the Kimmeridge sample (see organic petrography section above). However, spectra collected from within another bituminite fragment (Fig. 7C-D) showed a substantial range in λ_{max}, with values of approximately 562 nm (location 1), 523 nm (2), 534 nm (3), and 516 nm (4). These spectra show little variability in emission intensity and were therefore considered on average (539 nm, $n = 5$). This λ_{max} value converts to a BR_o value of 0.21% using the empirical calibration from Stasiuk (1994), lower than the measured value (0.29%), but much closer than calculated by application of the Hackley and Kus

(2015) calibration (0.45%). The closer correspondence of calculated BR_o values using data from stromatolitic *G. prisca* (from Stasiuk, 1994) suggest misapplication of the Hackley and Kus (2015) calibration from *Tasmanites* in bituminite studies.

3.2.1. Fluorescence alteration

Efforts to acquire three-dimensional CLSM imaging of bituminite in the KC-1 sample at University of Maryland resulted in unintentional photo-oxidation of the sample surface, i.e., a positive alteration (Davis et al., 1990; Ottenjann, 1988; Pradier et al., 1992). Positive alteration is a visual increase in fluorescence emission intensity, in this case after prolonged (14 min, 13 s) laser exposure (Fig. 8), and has been previously noted in the maceral bituminite (Sherwood and Cook, 1986).

The unintentional photo-oxidation provided opportunity to compare its effect on fluorescence color emission to adjacent unaffected areas. In
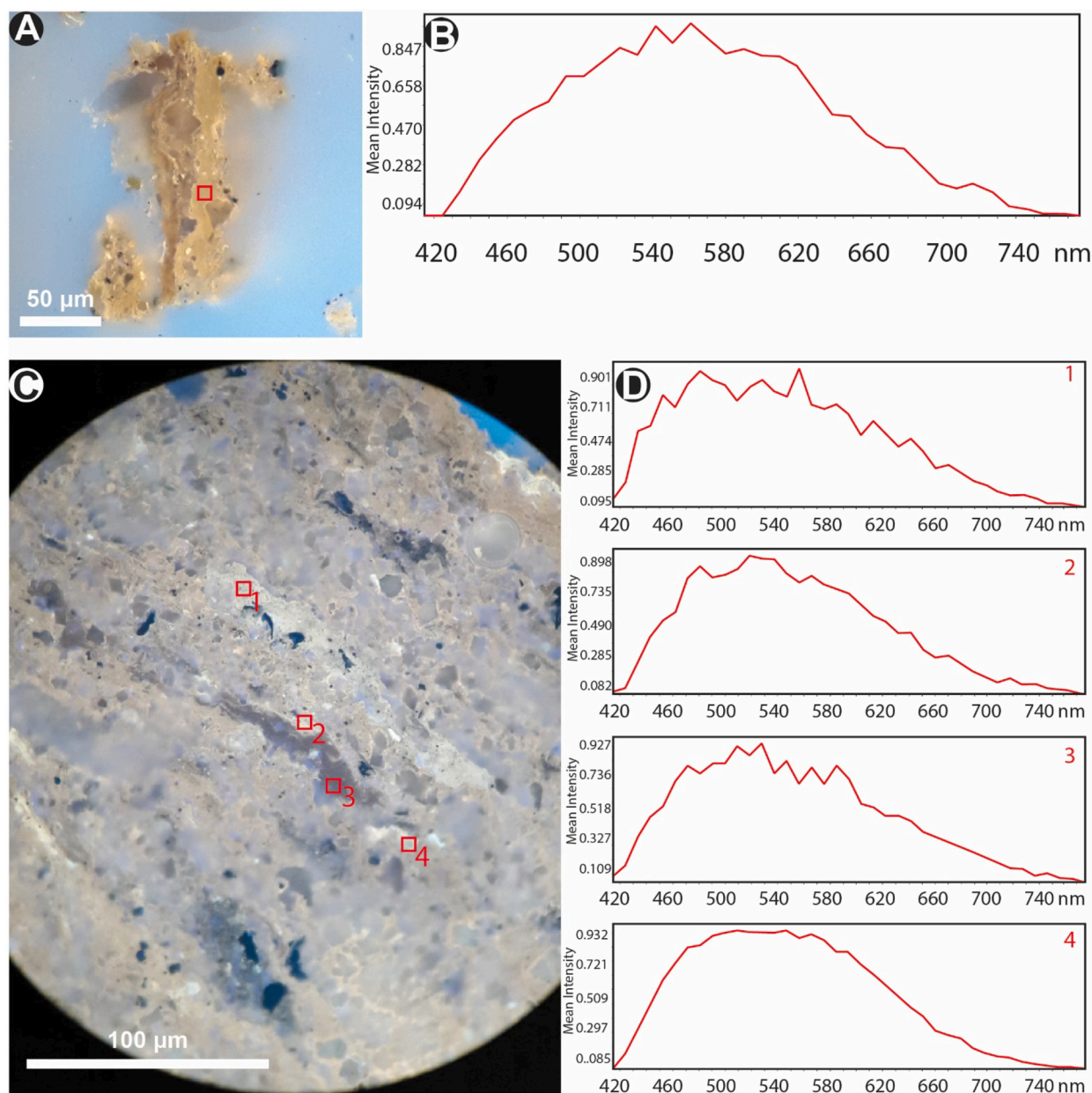
Fig. 7. Confocal laser scanning fluorescence spectroscopy data from bituminite in the KC-1 sample from INCAR. A. Fluorescence image of bituminite embedded in blue fluorescing epoxy-resin. B. Emission spectrum from region of interest (ROI) shown by red box in A. C. Fluorescence image of a second bituminite fragment, with 4 locations of spectral data collection annotated. D. Spectra from 4 locations marked in C. (For interpretation of the references to color in this figure legend, the reader is referred to the web version of this article.)

addition to the visual increase in emission intensity, photo-oxidation caused a blue shift in the wavelength of fluorescence emission. A large (~1600 μm^2) rectangular region of interest (ROI) shows average λ_{max} of 575 nm in an unaltered area, whereas average λ_{max} is blue-shifted to 540 nm in a similarly sized rectangular ROI in the adjacent area of photo-oxidation. This observation holds whether small or large ROIs are used for analysis. Fig. 8 also shows 10 circular ROIs of (~160 μm^2 each) in the unaltered area with average λ_{max} of 575–590 nm (overall average 581 nm), whereas 5 circular ROIs (~160 μm^2) in the area of photo-oxidation have average λ_{max} of 540 nm. Work on coal vitrinite and crude oil has established that positive alteration generally is associated with increased substitution of oxygen-containing moieties, e.g., car-boxylic acid groups (Davis et al., 1990), oxygen-substituted poly-aromatics (Pradier et al., 1990), or polyaromatics substituted with oxidized long chain aliphatics (Pradier et al., 1992). Regardless of the

type of substituted moiety, it is clear from multiple experimental studies that addition of surficial oxygen is responsible for the positive alteration occurring in photo-oxidation (Eberhardt et al., 1992; Mitchell et al., 2005).

Within both photo-oxidized and unaltered areas, fluorescence emission is blue-shifted in higher emission intensity areas relative to areas with lower emission intensity (Fig. 9). The absence of a preferred molecular orientation in bituminite (bituminite is without form by definition, Pickel et al., 2017), rules out alignment of the fluorophore transition moment with laser polarization (e.g., Hackley et al., 2020a), suggesting compositional differences cause the increased fluorophore yield and blue-shift (e.g., Hackley and Kus, 2015). This phenomenon may be related to the relative degradation of algal elements as discussed above in the imaging work from BGR. That is, areas of increased fluo-rophore yield and blue-shift are undegraded algal elements with specific
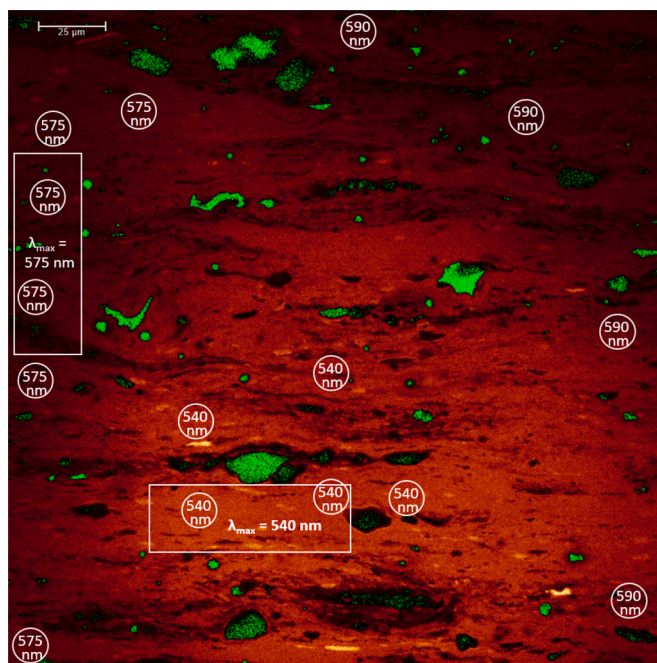
Fig. 8. Confocal laser scanning fluorescence spectroscopy data from bituminite in KC-1 sample from University of Maryland. Rectangular and circular regions of interest (ROIs) are labeled with average λ_{max} values from all pixels in the ROI. Note area of significant positive alteration in the lower center of the field and blue-shifted fluorescence emission in this area of higher emission intensity. (For interpretation of the references to color in this figure legend, the reader is referred to the web version of this article.)

Fig. 9. Photo-oxidized region from center of Fig. 8. Note consistent blue-shift in emission from areas of higher emission intensity. (For interpretation of the references to color in this figure legend, the reader is referred to the web version of this article.)
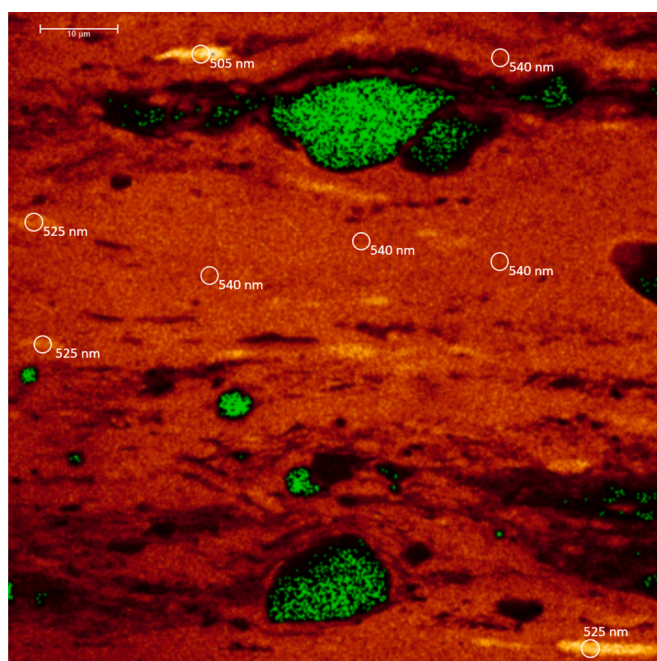
preserved fluorophore centers, whereas the overall bituminite is a mixture of many individual fluorophore types.

3.2.2. Need for standardization in CLSM fluorescence spectroscopy

Fluorescence spectroscopy at BGR used three laser lines (458 nm, 496 nm, and 633 nm) and the responses from all three were evaluated together over the emission range 400 to 800 nm. Ten locations were selected for measurement and averaged together, allowing estimation of a standard deviation as shown by the error bars in Fig. 10. One important artifact from this approach is the increased emission response at longer wavelengths due to application of the 633 nm laser, as noted in previous work (Hackley et al., 2020a). Nevertheless, the λ_{max} value of 562 nm from this approach is similar to that measured at University of Maryland (581 nm) and converts to a calculated BR_o value of 0.29% (using the calibration from Stasiuk, 1994), matching the measured BR_o value.

The different λ_{max} values obtained in this study [539 nm (INCAR), 562 nm (BGR), and 581 nm (Univ. MD)], and the different approaches used to derive the reported λ_{max} value, illustrate a continuing need for standardization in fluorescence spectroscopy of sedimentary organic matter (e.g., Hackley et al., 2020a). The lower average λ_{max} determined using the INCAR system ($\sim$539 nm) may possibly indicate stray light from blue fluorescing epoxy in the kerogen concentrate preparation, despite the fact that this value was obtained using a 405 diode laser for excitation, identical to the excitation wavelength used at Univ. MD, for which an average emission maximum of 581 nm was determined.

3.3. Atomic force microscopy

Previous investigations of bituminite in the KC-1 sample have shown a substantial increase in its reflectance following broad ion beam (BIB) milling sample preparation (Valentine et al., 2019). As shown in Fig. 11A-D, a selected region of bituminite increased in mean reflectance from 0.18% (s.d. 0.02, $n = 100$, Fig. 11A) to 0.38% (s.d. 0.03, n = 100, Fig. 11C) after BIB milling in a Hitachi IM 4000 Plus ion mill (milling conditions given in Materials and Methods section above). The increase in reflectance (0.20% absolute) was accompanied by a substantial decrease in areal root-mean-square surface roughness (S_q) of bituminite, as determined via atomic force microscopy (AFM), where lower values of S_q indicate flatter surfaces.

Areas of AFM topology data collection before and after BIB milling are shown as colored squares located over approximately the same location in bituminite before (Fig. 11B) and after (Fig. 11D) ion milling. Note the development of a gray reflecting surface in the bituminite in Fig. 11D, similar to the appearance of solid bitumen (Hackley et al., 2018). The regions of AFM data collection are shown as three-dimensional (3-D) representations in Fig. 11E-F. A ridge formed by the relative polishing relief of quartz is apparent post-milling near the right side of the 3-D image (Fig. 11F). In contrast, the adjacent softer bituminite is preferentially removed by BIB milling. The relative milling relief between bituminite and quartz results in an overall increase in S_q after milling, which is documented in Fig. 11G-H, where S_q increases from approximately 82 to 189 nm during milling. However, as highlighted by the three smaller regions of interest (ROI) in Fig. 11G-H, the bituminite experienced a relative decrease in S_q caused by the BIB milling, on average, from approximately 11 to 6 nm. The decrease in bituminite surface roughness is interpreted to cause its increased reflectance post-milling, as described in previous works (Grobe et al., 2017; Hackley et al., 2020b; Hackley et al., 2018; Valentine et al., 2019).

A separate, non-correlative AFM investigation of bituminite in the KC-1 sample showed overall increases in S_q after BIB milling. In this line of investigation, BIB milling of a mechanically polished sample surface used an E.A. Fischione 1060 SEM Mill (conditions given in Materials and Methods section). AFM data collection was on non-correlative locations, i.e., two samples were used: 1) mechanically polished (to 0.05 μm) KC-1, and 2) mechanically polished (also to 0.05 μm), and then BIB-milled KC-
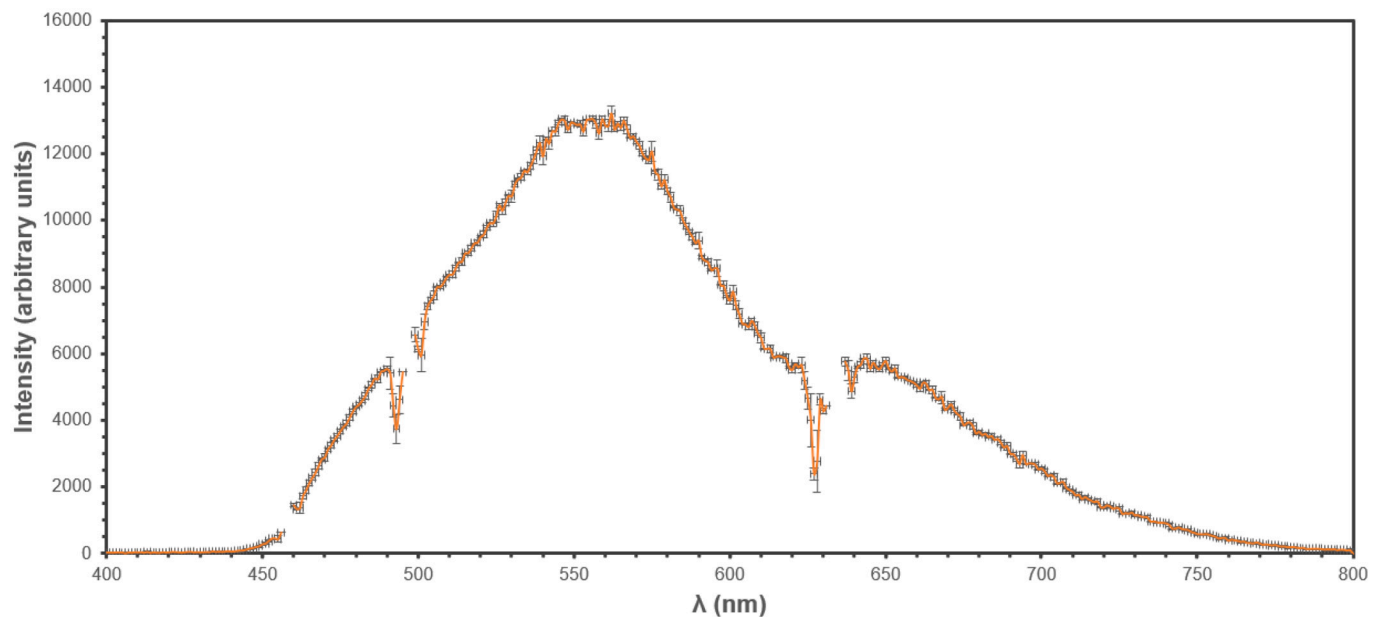
Fig. 10. Average bituminite emission spectrum measured at BGR, using 10 measurement locations and 3 laser lines. Error bars indicate standard deviation in measurement.

1. Collection of AFM data was on non-correlative locations of bituminite in the two samples. Whereas, in the preceding discussion, the AFM analysis was on a correlative location of bituminite before and after BIB milling. In the case where two samples were used (non-correlative locations), the mechanically polished surface (Fig. 12A-E) showed overall S_q values of 22 nm (20×20 μm field, Fig. 12A). Phase imaging of the same field (Fig. 12B) generally corresponds to the topographic image (Fig. 12A) suggesting a relatively homogeneous surface in terms of its mechanical properties (adhesion, stiffness, friction). This feature is further visualized in Fig. 12C where the phase image is laid over the topology in a 3-D view, showing that topographic depressions correspond to negative phase shift. Scratches from mechanical polish are apparent in the overlay, particularly in the lower half of the image. Sub-micron-sized sulfides (nano-sulfides) are present as finely disseminated inclusions in bituminite which polish out in relief during BIB milling (Fig. 12A-C). When progressively smaller and more homogeneous regions of interest (ROIs) were selected for analysis on the mechanically polished surface, even lower values of S_q were realized. For three 3×3 μm homogeneous ROIs selected within the 20×20 μm field, S_q values of 4–8 nm were measured (Fig. 12E). The trend of lower S_q values from smaller fields continues at another location in the mechanically polished sample (Fig. 13A-E). Fig. 13A shows an overall S_q of 9.6 nm for a 6.25×6.25 μm field (Fig. 13A), and still lower values of 1.80–2.44 nm for 950×950 nm ROIs (Fig. 13E). Phase imaging (Fig. 13B) again corresponds to topology (Fig. 13C), indicating homogeneity in mechanical properties of the surface.

The non-correlative BIB-milled KC-1 sample surface showed higher S_q values of 121 nm (70×70 μm field, Fig. S1), 108 nm (50×50 μm field, Fig. S2), and 136 nm (12×12 μm field, Fig. 14A-D). Fig. 14A shows ion-induced exposure of disseminated nano-sulfides in the sample surface and a much wider expression of phase shift (Fig. 14B) than in mechanically polished surfaces, related to the increased exposure of nano-sulfides, which show a positive phase shift relative to the bituminite. Scratches from mechanical polish are no longer apparent; instead, curtaining effects are present as aligned troughs in bituminite. Similar to the mechanically polished surface, smaller homogeneous ROIs of 1.5×1.5 μm within the 12×12 μm field showed lower S_q values of 10.7–16.8 nm (Fig. 14E), indicating measurement of surface roughness for petrographic preparations of the KC-1 sample is strongly dependent on the scale of observation, whether in mechanically polished or ion-milled surfaces. The smaller (1.5×1.5 μm) ROIs are, however, an order of magnitude rougher than similar sized areas in the mechanically polished surface. This increase in surface roughness (increase in S_q) after BIB-milling (with the Fischione mill and its corresponding milling conditions) is interpreted to reflect the relief created by differential milling and removal of the bituminite compared to its nano-sulfide inclusions. We hypothesize this was caused by ion erosion of the softer bituminite, exposing the embedded nano-sulfides and thus creating relief measured as higher S_q values. An identical effect was described above in the correlative AFM investigation for preferential removal of bituminite relative to quartz, illustrated as a quartz ridge in Fig. 11D, F, and H, and a higher S_q value in the post-milled whole field area of data collection.

Mechanical polish of bituminite may 'smear' the soft organic matter over and around harder, embedded nano-sulfides, disguising their presence and reducing measured relief in the mechanically polished surface. Because the work using the Fischione mill was a non-correlative investigation (the same location was not investigated before and after BIB-milling), it is also possible that the consistently higher values of S_q in the milled sample may reflect locational differences in the material analyzed between the milled and non-milled samples. Nevertheless, the contradictory results between the correlative (lower S_q after BIB milling) and non-correlative (higher S_q after BIB milling) AFM investigations highlight our still limited understanding of the effects of BIB milling to sedimentary organic matter (Hackley et al., 2020b), and show the need for further research before BIB milling can be advanced as a standard practice in sample preparation of sedimentary organic matter such as bituminite.

4. Summary

Confocal laser scanning microscopy (CLSM) imaging and spectroscopy and atomic force microscopy (AFM) were used for characterization of bituminite in an organic-rich, immature sample from the Kimmeridge Clay Formation. Key findings from two- and three-dimensional CLSM imaging included:

1. incomplete blocking of reflected laser light from low-absorbing sulfide and fusinite inclusions in bituminite;
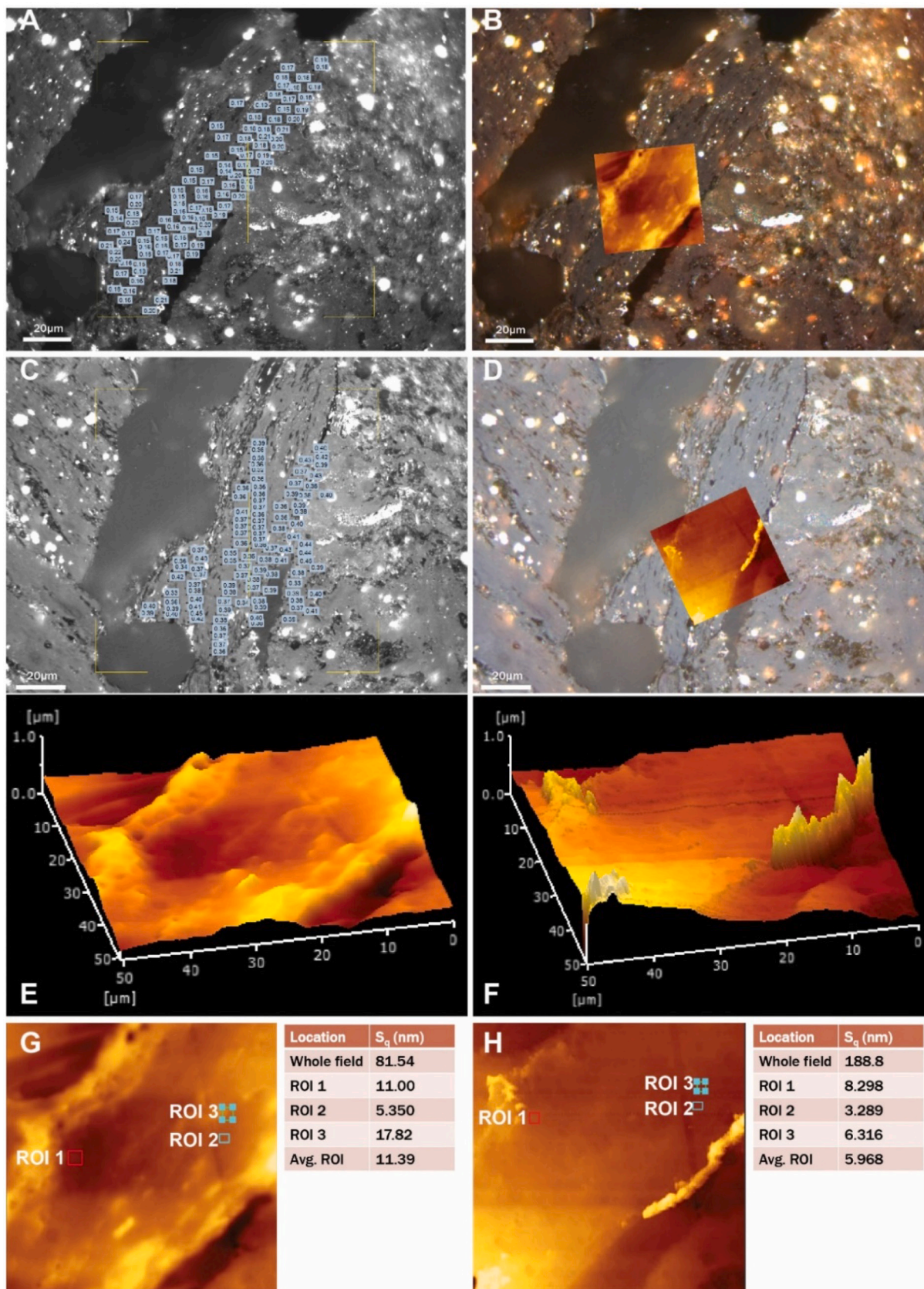
Fig. 11. Reflectance increase and surface flattening of bituminite in the mechanically polished KC-1 sample caused by broad ion beam (BIB) milling. A. Reflectance of mechanically polished bituminite pre-BIB milling, monochrome. B. Same field as A with atomic force microscopy (AFM) overlay, color. C. Reflectance of bituminite post-BIB milling, monochrome. D. Same field as C with AFM overlay, color. E. 3D representation of AFM topology, pre-BIB milling. F. 3D representation of AFM topology, post-BIB milling. G. AFM topology pre-BIB milling showing 3 regions of interest (ROI) in bituminite and corresponding S_q values. H. AFM topology post-BIB milling showing 3 regions of interest (ROI) in bituminite and corresponding S_q values.
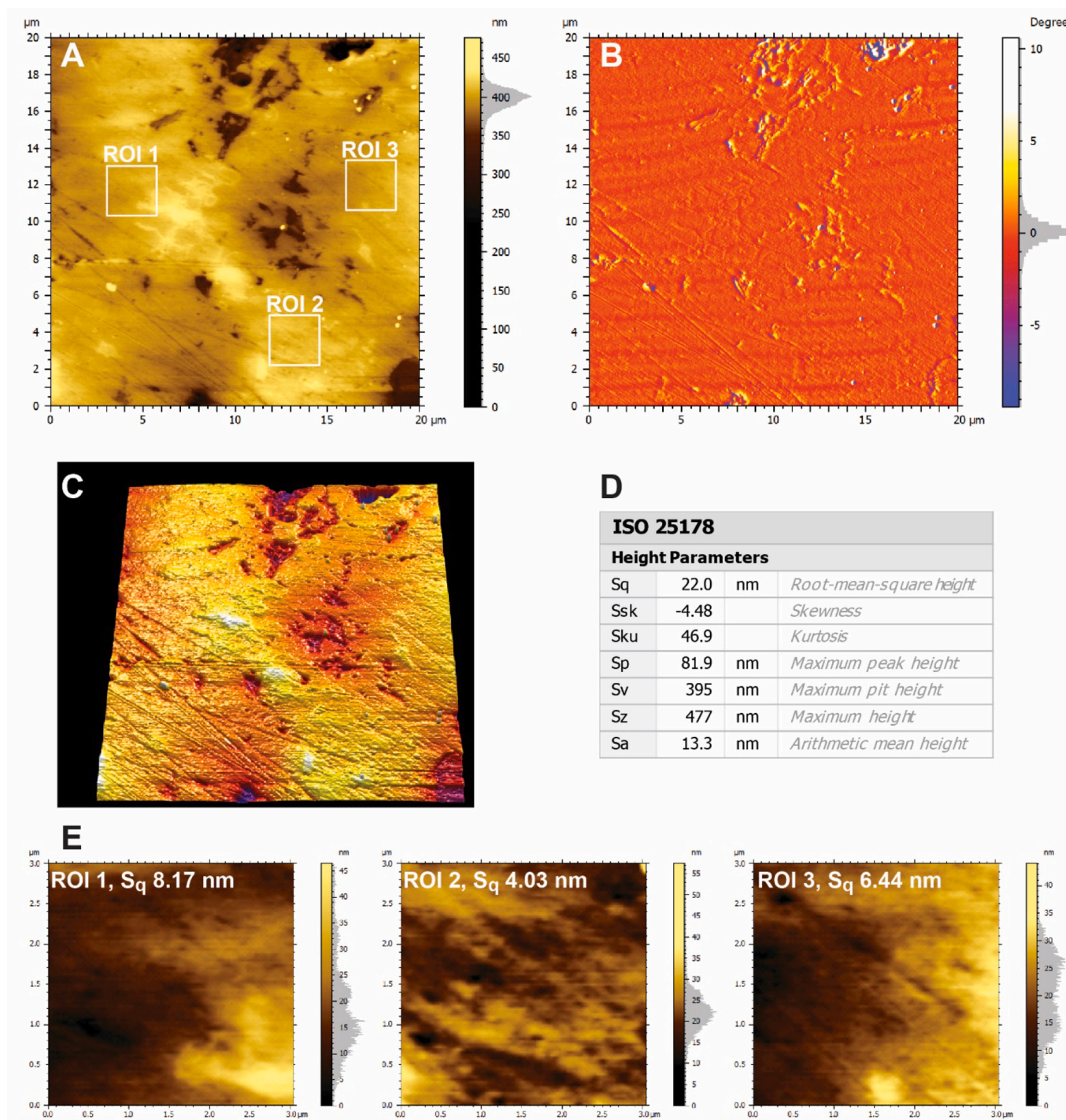
Fig. 12. Atomic force microscopy (AFM) data from bituminite in mechanically polished KC-1 sample. A. AFM topography of 20 × 20 μm field. B. AFM phase contrast of same field as A. C. Phase contrast overlaid on 3-D topology. D. Surface parameters calculated as per (ISO, 2012). E. AFM topography from three 3 × 3 μm regions of interest (ROI) shown in A.

2. radiation halos of decreased fluorescence intensity around radioactive minerals in bituminite;

3. the presence of sporinite and *Botryococcus* (interpreted identification) as particulate constituents of bituminite;

4. and the red-shift of sulfide reflectance and bituminite fluorescence from below the sample surface.

Findings from CLSM spectroscopy included:

5. color blue-shift from positive alteration via laser-induced photo-oxidation of bituminite;

6. blue-shift associated to higher fluorescence intensity regions in bituminite, probably due to differences in composition, e.g., related to particulate constituents or degradation products thereof;

7. differences in spectroscopic data collection procedures and reported fluorescence emission parameters for bituminite, highlighting the need for standardization in fluorescence spectroscopy;
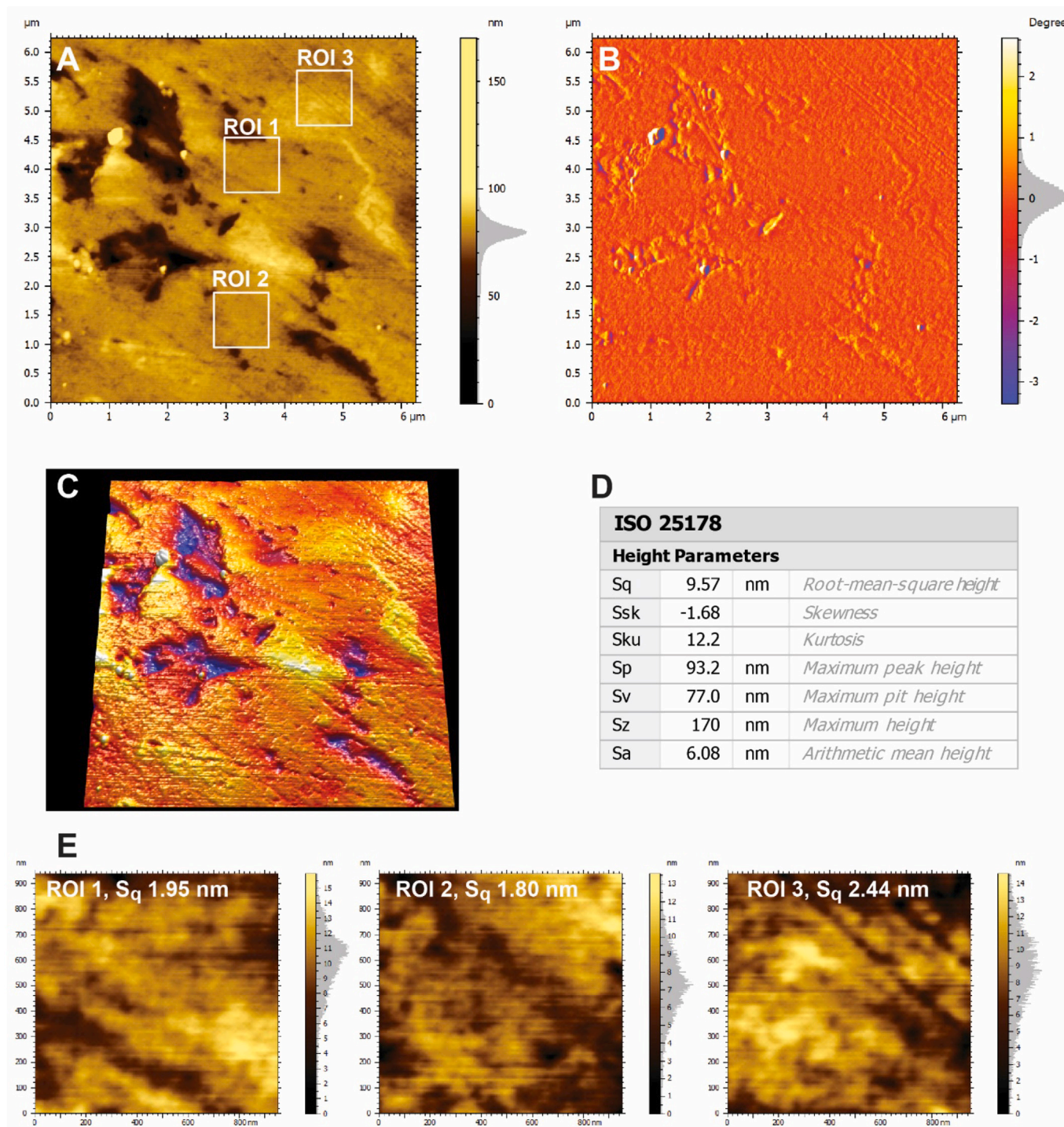
Fig. 13. Atomic force microscopy (AFM) data from bituminite in mechanically polished KC-1 sample. A. AFM topography of 6.25 × 6.25 μm field. B. AFM phase contrast of same field as A. C. Phase contrast overlaid on 3-D topology. D. Surface parameters for 6.25 × 6.25 μm field calculated as per (ISO, 2012). E. AFM topography from three 950 × 950 nm regions of interest (ROI) shown in A.

8. and the prediction of solid bitumen reflectance via calibration to an extant dataset.

Findings from AFM included:

9. increased surface flattening from broad ion beam (BIB) milling which resulted in higher reflectance of bituminite;
10. the differential ion erosion of bituminite compared to harder micro- and nanoscale quartz and sulfide inclusions;
11. the exposure by BIB milling of nano-sulfides embedded in bituminite which resulted in decreased surface flatness.
12. and that the magnitude of bituminite surface deviation from perfect flatness was dependent on the scale of observation.

These findings illustrate the utility of CLSM and AFM as research tools in organic petrology, and suggest that future workers could leverage the investigative properties of both approaches in combined AFM-CLSM studies of bituminite. The identification of figured liptinite
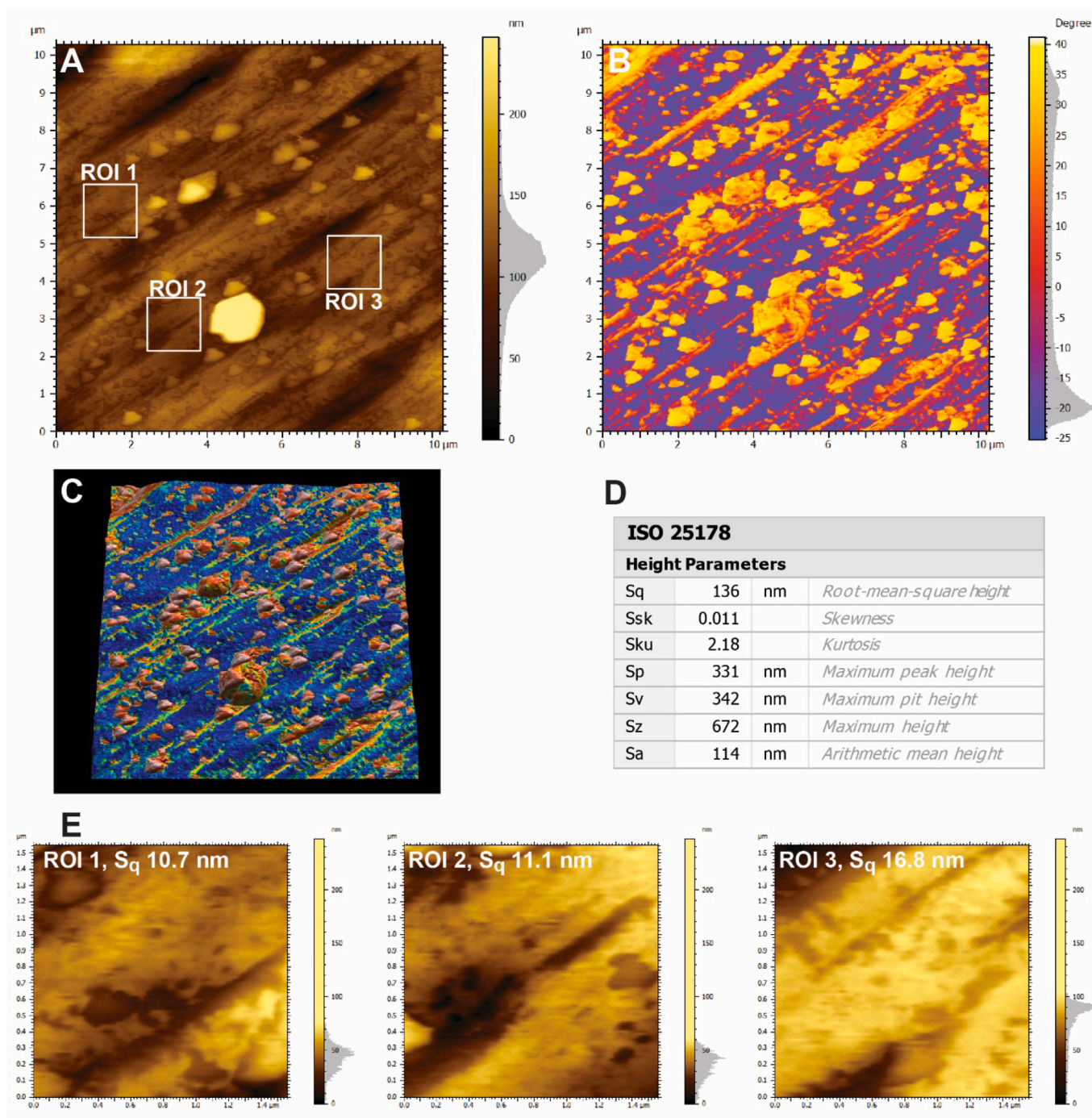
Fig. 14. Atomic force microscopy (AFM) data from bituminite in mechanically polished, then BIB-milled KC-1 sample. A. AFM topography of 12 × 12 μm field. B. AFM phase contrast of same field as A. C. Phase contrast overlaid on 3-D topology. D. Surface parameters for 12 × 12 μm field calculated as per (ISO, 2012). E. AFM topography from three 1.5 × 1.5 μm regions of interest (ROI) shown in A.

inclusions (i.e., sporinite, *Botryococcus*) in bituminite may point to improved imaging capability over conventional epi-fluorescence, and the prediction of solid bitumen reflectance via spectroscopy further illustrates potential applications of CLSM as a thermal probe in low maturity settings. However, detection of reflected laser light and variability of fluorescence emission parameters dependent on data collection protocol suggest caution is needed in CLSM spectroscopy applications. The observation from AFM that surficial alteration caused by BIB milling is dependent on the scale of observation also indicates the need for future standardization in sample preparation. Overall, this work illustrates some advantages and limitations in application of state-of-the-art CLSM and AFM technologies for organic petrology research.

Author contributions

PCH and JK conceived the investigation of bituminite via CLSM. JGMF performed kerogen isolation. ADC, AGB, DZ, PCH and JK collected CLSM data. BJV performed BIB milling. PCH, BJV and JJH collected AFM data. JJH performed sample preparation. PCH wrote the manuscript with input from all co-authors.

Declaration of Competing Interest

Acknowledgements

Appendix A. Supplementary data

Supplementary data to this article can be found online at https://doi.org/10.1016/j.coal.2022.103927.

References

ASTM, 2015a. D2797 Standard Practice for Preparing Coal Samples for Microscopical Analysis by Reflected Light, Petroleum Products, Lubricants, and Fossil Fuels; Gaseous Fuels; Coal and Coke, Sec. 5, v. 05.06. ASTM International, West Conshohocken, PA.

ASTM, 2015b. D7708 Standard Test Method for Microscopical Determination of the Reflectance of Vitrinite Dispersed in Sedimentary Rocks, Petroleum Products, Lubricants, and Fossil Fuels; Gaseous Fuels; Coal and Coke, Sec. 5, v. 05.06. ASTM International, West Conshohocken, PA.

Binnig, G., Quate, C.F., Gerber, C., 1986. Atomic force microscope. Phys. Rev. Lett. 56, 930–933.

Birdwell, J.E., Washburn, K.E., 2015. Rapid analysis of kerogen hydrogen-to-carbon ratios in shale and mudrocks by laser-induced breakdown spectroscopy. Energy Fuel 29, 6999–7004.

Bolin, T.B., Birdwell, J.E., Lewan, M.D., Hill, R.J., Grayson, M.B., Mitra-Kirtley, S., Bake, K.D., Craddock, P.R., Abdallah, W., Pomerantz, A.E., 2016. Sulfur species in source rock bitumen before and after hydrous pyrolysis determined by X-ray absorption near-edge structure. Energy Fuel 30, 6264–6270.

Botz, R., Schmidt, M., Wehner, H., Hufnagel, H., Stoffers, P., 2007. Organic-rich sediments in brine-filled Shaban- and Kebrit deeps, northern Red Sea. Chem. Geol. 244, 520–553.

Boucsein, B., Stein, R., 2009. Black shale formation in the late Paleocene/early Eocene Arctic Ocean and paleoenvironmental conditions: new results from a detailed organic petrological study. Mar. Pet. Geol. 26, 416–426.

Boussafir, M., Gelin, F., Lallier-Vergès, E., Derenne, S., Bertrand, P., Largeau, C., 1995. Electron microscopy and pyrolysis of kerogens from the Kimmeridge Clay Formation, UK: source organisms, preservation processes, and origin of microcycles. Geochim. Cosmochim. Acta 59, 3731–3747.

Burnham, A.K., 2019. Kinetic models of vitrinite, kerogen, and bitumen reflectance. Org. Geochem. 131, 50–59.

Chadwick, R.A., 1986. Extension tectonics in the Wessex Basin, southern England. J. Geol. Soc. 143, 465–488.

Creaney, S., 1980. The organic petrology of the Upper Cretaceous Boundary Creek Formation, Beaufort-Mackenzie Basin. Bull. Can. Petrol. Geol. 28, 112–119.

Czaja, A.D., Beukes, N.J., Osterhout, J.T., 2016. Sulfur-oxidizing bacteria prior to the Great Oxidation Event from the 2.52 Ga Gamohaan Formation of South Africa. Geology 44, 983–986.

Davis, A., Rathbone, R.F., Lin, R., Quick, J.C., 1990. Observations concerning the nature of maceral fluorescence alteration with time. Org. Geochem. 16, 897–906.

Eberhardt, J.E., Nguyen, T.H., Read, R., 1992. Fluorescence alteration of coal and polycyclic aromatic hydrocarbons. Org. Geochem. 18, 145–153.

Eble, C.F., 2012. Organic petrology of Carbondale Formation coal beds and marine roof shales in Western Kentucky, Eastern Interior (Illinois) Basin, USA. Int. J. Coal Geol. 104, 60–69.

Eliyahu, M., Emmanuel, S., Day-Stirrat, R.J., Macaulay, C.I., 2015. Mechanical properties of organic matter in shales mapped at the nanometer scale. Mar. Pet. Geol. 59, 294–304.

Emmanuel, S., Eliyahu, M., Day-Stirrat, R.J., Hofmann, R., Macaulay, C.I., 2016. Impact of thermal maturation on nano-scale elastic properties of organic matter in shales. Mar. Pet. Geol. 70, 175–184.

Ettensohn, F.R., 1998. Compressional tectonic controls on epicontinental black-shale deposition: Devonian-Mississippian examples from North America. In: Scheiber, J., Zimmerle, W., Sethi, P.S. (Eds.), Shales and Mudstones, I: Basin Studies, Sedimentology, and Paleontology. E Schweizerbart'sche Verlagsbuchhandlung Naegele u. Obermiller, Stuttgart, pp. 109–128.

Faraj, B.S.M., Mackinnon, I.D.R., 1993. Micrinite in Southern Hemisphere sub-bituminous and bituminous coals: redefined as fine grained kaolinite. Org. Geochem. 20, 823–841.

Fishman, N.S., Hackley, P.C., Lowers, H.A., Hill, R.J., Egenhoff, S.O., Eberl, D.D., Blum, A.E., 2012. The nature of porosity in organic-rich mudstones of the Upper Jurassic Kimmeridge Clay Formation, North Sea, offshore United Kingdom. Int. J. Coal Geol. 103, 32–50.

Gadelmawla, E.S., Koura, M.M., Maksoud, T.M.A., Elewa, I.M., Soliman, H.H., 2002. Roughness parameters. J. Mater. Process. Technol. 123, 133–145.

Geršlová, E., Opletal, V., Sýkorová, I., Sedláková, I., Geršl, M., 2015. A geochemical and petrographical characterization of organic matter in the Jurassic Mikulov Marls from the Czech Republic. Int. J. Coal Geol. 141-142, 42–50.

Grobe, A., Schmatz, J., Littke, R., Klaver, J., Urai, J.L., 2017. Enhanced surface flatness of vitrinite particles by broad ion beam polishing and implications for reflectance measurements. Int. J. Coal Geol. 180, 113–121.

Hackley, P.C., Kus, J., 2015. Thermal maturity of *Tasmanites* microfossils from confocal laser scanning fluorescence microscopy. Fuel 143, 343–350.

Hackley, P.C., SanFilipo, J.R., 2016. Organic petrology and geochemistry of Eocene Suzak bituminous marl, north-central Afghanistan: depositional environment and source rock potential. Mar. Pet. Geol. 73, 572–589.

Hackley, P.C., Fishman, N., Wu, T., Baugher, G., 2016. Organic petrology and geochemistry of mudrocks from the lacustrine Lucaogou Formation, Santanghu Basin, northwest China: Application to lake basin evolution. Int. J. Coal Geol. 168, 20–34.

Hackley, P.C., Valentine, B.J., Hatcherian, J.J., 2018. On the petrographic distinction of bituminite from solid bitumen in immature to early mature source rocks. Int. J. Coal Geol. 196, 232–245.

Hackley, P.C., Jubb, A.M., Burruss, R.C., Beaven, A.E., 2020a. Fluorescence spectroscopy of ancient sedimentary organic matter via confocal laser scanning microscopy (CLSM). Int. J. Coal Geol. 223, 103445.

Hackley, P.C., Jubb, A.M., Valentine, B.J., Hatcherian, J.J., Yu, J.-J., Podrazky, W.K., 2020b. Investigating the effects of broad ion beam milling to sedimentary organic matter: surface flattening or heat-induced aromatization and condensation? Fuel 282.

Hackley, P.C., Jubb, A.M., McAleer, R.J., Valentine, B.J., Birdwell, J.E., 2021. A review of spatially resolved techniques and applications of organic petrography in shale petroleum systems. Int. J. Coal Geol. 241, 103745.

Hackley, P.C., Kus, J., Mendonça Filho, J.G., Czaja, A.D., Borrego, A.G., Životić, D., Valentine, B.J., Hatcherian, J.J., 2022. Reflectance and Confocal Laser Scanning Fluorescence Spectroscopy of Bituminite in Kimmeridge Clay: U.S. Geological Survey Data Release. https://doi.org/10.5066/P9RW8JRH.

Hutton, A.C., Kantsler, A.J., Cook, A.C., McKirdy, D.M., 1980. Organic matter in oil shales. APEA J. 20, 44–67.

Hutton, A., Bharati, S., Robl, T., 1994. Chemical and petrographic classification of kerogen/macerals. Energy Fuel 8, 1478–1488.

ICCP, 2001. The new inertinite classification (ICCP System 1994). Fuel 80, 459–471.

ISO, 2012. 25178-2 Geometric Product Specifications (GPS) - Surface Texture, Areal: Part 2, Terms, Definitions and Surface Texture Parameters. ISO, p. 47.

Kempe, A., Schopf, J.W., Altermann, W., Kudryavtsev, A.B., Heckl, W.M., 2002. Atomic force microscopy of Precambrian microscopic fossils. Proc. Natl. Acad. Sci. U. S. A. 99, 9117–9120.

Kolonic, S., Sinninghe Damsté, J., Böttcher, M.E., Kuypers, M.M.M., Kuhnt, W., Beckmann, B., Scheeder, G., Wagner, T., 2002. Geochemical characterization of Cenomanian/Turonian black shales from the Tarfaya Basin (SW Morocco): relationships between paleoenvironmental conditions and early sulfurization of sedimentary organic matter. J. Pet. Geol. 25, 325–350.

Kus, J., 2015. Application of confocal laser-scanning microscopy (CLSM) to autofluorescent organic and mineral matter in peat, coals and siliciclastic sedimentary rocks — a qualitative approach. Int. J. Coal Geol. 137, 1–18.

Kus, J., Khanaqa, P., Mohialdeen, I.M.J., Kaufhold, S., Babies, H.G., Meßner, J., Blumenberg, M., 2016. Solid bitumen, bituminite and thermal maturity of the Upper Jurassic-Lower Cretaceous Chia Gara Formation, Kirkuk Oil Field, Zagros Fold Belt, Kurdistan, Iraq. Int. J. Coal Geol. 165, 28–48.

Kus, J., Araujo, C.V., Borrego, A.G., Flores, D., Hackley, P.C., Hámor-Vidó, M., Kalaitzidis, S., Kommeren, C.J., Kwiecińska, B., Mastalerz, M., Mendonça Filho, J.G., Menezes, T.R., Misz-Kennan, M., Nowak, G.J., Petersen, H.I., Rallakis, D., Suárez-Ruiz, I., Sýkorová, I., Životić, D., 2017. Identification of alginite and bituminite in rocks other than coal. 2006, 2009, and 2011 round robin exercises of the ICCP Identification of Dispersed Organic Matter Working Group. Int. J. Coal Geol. 178, 26–38.

Lees, J.A., Bown, P.R., Young, J.R., Riding, J.B., 2004. Evidence for annual records of phytoplankton productivity in the Kimmeridge Clay Formation coccolith stone bands (Upper Jurassic, Dorset, UK). Mar. Micropaleontol. 52, 29–49.

Lees, J.A., Bown, P.R., Young, J.R., 2006. Photic zone palaeoenvironments of the Kimmeridge Clay Formation (Upper Jurassic, UK) suggested by calcareous nannoplankton palaeoecology. Palaeogeogr. Palaeoclimatol. Palaeoecol. 235, 110–134.

Luo, Q., Zhong, N., Qin, J., Li, K., Zhang, Y., Wang, Y., Ma, L., 2014. Thucholite in Mesoproterozoic shales from northern north China: occurrence and indication for thermal maturity. Int. J. Coal Geol. 125, 1–9.

Machovic, V., Havelcova, M., Sykorova, I., Borecka, L., Lapcak, L., Mizera, J., Kribek, B., Krist, P., 2021. Raman mapping of coal halos induced by uranium mineral radiation. Spectrochim. Acta A Mol. Biomol. Spectrosc. 246, 118996.

Masters, M.J., 1971. The occurrence of *Chytridium marylandicum* on *Botryococcus braunii* in School Bay of the Delta Marsh. Can. J. Bot. 49, 1479–1485.

Mendonça Filho, J.G., Menezes, T.R., Mendonça, J.O., 2017. 10th ICCP Training Course on Dispersed Organic Matter Integrating Transmitted and Reflected Light Microscopy. ICCP, Potsdam, Germany.

Metzger, P., Largeau, C., 2005. Botryococcus braunii: a rich source for hydrocarbons and related ether lipids. Appl. Microbiol. Biotechnol. 66, 486–496.

Mitchell, G.D., Davis, A., Chander, S., 2005. Surface properties of photo-oxidized bituminous vitrains. Int. J. Coal Geol. 62, 33–47.

Mukhopadhyay, P.K., Hagemann, H.W., Gormly, J.R., 1985. Characterization of kerogens as seen under the aspects of maturation and hydrocarbon generation. Erdöl und Kohle, Erdgas, Petrochemie 38, 7–18.

Nix, T., Feist-Burkhardt, S., 2003. New methods applied to the microstructure analysis of Messel oil shale: confocal laser scanning microscopy (CLSM) and environmental scanning electron microscopy (ESEM). Geol. Mag. 140, 469–478.

Nowak, G.J., 2007. Comparative studies of organic matter petrography of the late palaeozoic black shales from Southwestern Poland. Int. J. Coal Geol. 71, 568–585.

Ottenjann, K., 1988. Fluorescence alteration and its value for studies of maturation and bituminization. Org. Geochem. 12, 309–321.

Pacton, M., Fiet, N., Gorin, G.E., 2007. Bacterial activity and preservation of sedimentary organic matter: the role of exopolymeric substances. Geomicrobiol J. 24, 571–581.

Pickel, W., Kus, J., Flores, D., Kalaitzidis, S., Christanis, K., Cardott, B.J., Misz-Kennan, M., Rodrigues, S., Hentschel, A., Hamor-Vido, M., Crosdale, P., Wagner, N., 2017. Classification of liptinite – ICCP System 1994. Int. J. Coal Geol. 169, 40–61.

Powell, T.G., Creaney, S., Snowdon, L.R., 1982. Limitations of use of organic petrographic techniques for identification of petroleum source rocks. Am. Assoc. Pet. Geol. Bull. 66, 430–435.

Pradier, B., Largeau, C., Derenne, S., Martinez, L., Bertrand, P., Pouet, Y., 1990. Chemical basis of fluorescence alteration of crude oils and kerogens-I. Microfluorimetry of an oil and its isolated fractions; relationships with chemical structure. Org. Geochem. 16, 451–460.

Pradier, B., Landais, P., Rochdi, A., Davis, A., 1992. Chemical basis of fluorescence alteration of crude oils and kerogens II. Fluorescence and infrared micro-spectrometric analysis of vitrinite and liptinite. Org. Geochem. 18, 241–248.

Rao, A.R., Dayananda, C., Sarada, R., Shamala, T.R., Ravishankar, G.A., 2007. Effect of salinity on growth of green alga *Botryococcus braunii* and its constituents. Bioresour. Technol. 98, 560–564.

Rimmer, S.M., Thompson, J.A., Goodnight, S.A., Robl, T.L., 2004. Multiple controls on the preservation of organic matter in Devonian-Mississippian marine black shales: geochemical and petrographic evidence. Palaeogeogr. Palaeoclimatol. Palaeoecol. 215, 125–154.

Ross, D.J.K., Bustin, R.M., 2006. Sediment geochemistry of the Lower Jurassic Gordondale Member, northeastern British Columbia. Bull. Can. Petrol. Geol. 54, 337–365.

Schopf, J.W., Kudryavtsev, A.B., 2009. Confocal laser scanning microscopy and Raman imagery of ancient microscopic fossils. Precambrian Res. 173, 39–49.

Schopf, J.W., Kudryavtsev, A.B., Sugitani, K., Walter, M.R., 2010. Precambrian microbe-like pseudofossils: a promising solution to the problem. Precambrian Res. 179, 191–205.

Schopf, J.W., Kudryavtsev, A.B., Tripathi, A.B., Czaja, A.D., 2011. Three-dimensional morphological (CLSM) and chemical (Raman) imagery of cellularly mineralized fossils. In: Allison, P.A., Bottjer, D.J. (Eds.), Taphonomy: Process and Bias Through Time, 2nd ed. Springer, Dordrecht, pp. 457–486.

Schopf, J.W., Sergeev, V.N., Kudryavtsev, A.B., 2016. A new approach to ancient microorganisms: taxonomy, paleoecology, and biostratigraphy of the Lower Cambrian Berkuta and Chulaktau microbiotas of South Kazakhstan. J. Paleontol. 89, 695–729.

Sherwood, N., Cook, A.C., 1986. Organic matter in the Toolebuc Formation. In: Gravestock, D.I., Moore, P.S., Pitt, G.M. (Eds.), Contributions to the Geology and Hydrocarbon Potential of the Eromanga Basin. Geological Society of Australia Special Publication, vol. 12, pp. 255–265.

Stasiuk, L.D., 1993. Algal bloom episodes and the formation of bituminite and micrinite in hydrocarbon source rocks: evidence from the Devonian and Mississippian, northern Williston Basin, Canada. Mar. Pet. Geol. 11, 219–231.

Stasiuk, L.D., 1994. Fluorescence properties of Palaeozoic oil-prone alginite in relation to hydrocarbon generation, Williston Basin, Saskatchewan, Canada. Mar. Pet. Geol. 11, 219–231.

Stasiuk, L.D., 1999. Confocal laser scanning fluorescence microscopy of *Botryococcus* alginite from boghead oil shale, Boltysk, Ukraine: selective preservation of various micro-algal components. Org. Geochem. 30, 1021–1026.

Stasiuk, L.D., Goodarzi, F., 1988. Organic petrology of second white speckled shale, Saskatchewan, Canada: a possible link between bituminite and biogenic gas? Bull. Can. Petrol. Geol. 36, 397–406.

Stasiuk, L.D., Sanei, H., 2001. Characterization of diatom-derived lipids and chlorophyll within Holocene laminites, Saanich Inlet, British Columbia, using conventional and laser scanning fluorescence microscopy. Org. Geochem. 32, 1417–1428.

Synnott, D.P., Sanei, H., Dewing, K., Ardakani, O.H., Pedersen, P.K., 2017. Insight into visible light spectrum changes with increasing reflectance in bituminite and inertinite macerals. Fuel 197, 201–208.

Tao, S., Wang, Y., Tang, D., Wu, D., Xu, H., He, W., 2012. Organic petrology of Fukang Permian Lucaogou Formation oil shales at the northern foot of Bogda Mountain, Junggar Basin, China. Int. J. Coal Geol. 99, 27–34.

Taylor, G.H., Liu, S.Y., Teichmüller, M., 1991. Bituminite - a TEM view. Int. J. Coal Geol. 18, 71–85.

Taylor, G.H., Teichmüller, M., Davis, A., Diessel, C.F.K., Littke, R., Robert, P., 1998. Organic Petrology. Gebruder Borntraeger, Berlin and Stuttgart.

Teichmüller, M., 1971. Anwendung kohlenpetrographischer methoden bei der erdoel und erdgasprospektion. Erdol, Kohle, Erdgas, Petrochemie 24, 69–76.

Teichmüller, M., 1974a. Enstehung und veränderung bituminöser substanzen in kohlen in beziehung zur entstehung und umwandlung des erdöls. Forschr. Geol. Rheinl. Westfalen 24.

Teichmüller, M., 1974b. Über neue Macerale der Liptinit-Gruppe und die Entstehung des Micrinits. Fortschr. Geol. Rheinl. Westfalen 24, 37–64.

Teichmüller, M., Ottenjann, K., 1977. Art und Diagenese von Liptiniten und lipoiden Stoffen in einem Erdölmuttergestein aufgrund fluoreszenzmikroskopischer Untersuchungen. Erdol, Kohle, Erdgas, Petrochem. 30, 387–398.

Teng, J., Mastalerz, M., Liu, B., 2021. Petrographic and chemical structure characteristics of amorphous organic matter in marine black shales: insights from Pennsylvanian and Devonian black shales in the Illinois Basin. Int. J. Coal Geol. 235.

Tribovillard, N.-P., Desprairies, A., Lallier-Vergès, E., Bertrand, P., Moureau, N., Ramdani, A., Ramanampisoa, L., 1994. Geochemical study of organic-matter rich cycles from the Kimmeridge Clay Formation of Yorkshire (UK): productivity versus anoxia. Palaeogeogr. Palaeoclimatol. Palaeoecol. 106, 165–181.

Tyson, R.V., 1995. Sedimentary Organic Matter. Chapman and Hall, London.

Valentine, B.J., Hackley, P.C., Hatcherian, J., Yu, J.-J., 2019. Reflectance increase from broad beam ion milling of coals and organic-rich shales due to increased surface flatness. Int. J. Coal Geol. 201, 86–101.

van Gijzel, P., 1981. Applications of geomicrophotometry of kerogen, solid hydrocarbons and crude oils to petroleum exploration. In: Brooks, J. (Ed.), Organic Maturation Studies and Fossil Fuel Exploration. Academic Press, New York, pp. 351–377.

Vandenbroucke, M., Largeau, C., 2007. Kerogen origin, evolution and structure. Org. Geochem. 38, 719–833.

Wang, K., Taylor, K.G., Ma, L., 2021. Advancing the application of atomic force microscopy (AFM) to the to the characterization and quantification of geological material properties. In: International Journal of Coal Geology TBD. TBD.

Webb, R.H., 1996. Confocal optical microscopy. Rep. Prog. Phys. 59, 427–471.

Williams, P.F.V., Douglas, A.G., 1980. A preliminary organic geochemical investigation of the Kimmeridgian oil shales. Phys. Chem. Earth 12, 531–545.

Zheng, X., Schovsbo, N.H., Bian, L., Luo, Q., Zhong, N., Rudra, A., Goodarzi, F., Sanei, H., 2021. Alteration of organic macerals by uranium irradiation in lower Paleozoic marine shales. Int. J. Coal Geol. 239, 103713.